9

Computational Infrastructure for the Real-Time Patient-Specific Treatment of Cancer

K. R. Diller, J. T. Oden, C. Bajaj, J. C. Browne,
J. Hazle, I. Babuška, J. Bass, L. Bidaut,
L. Demkowicz, A. Elliott, Y. Feng, D. Fuentes,
S. Goswami, A. Hawkins, S. Khoshnevis,
B. Kwon, S. Prudhomme, and R. J. Stafford

CONTENTS

9.1   INTRODUCTION

The computational control system under development at the University of Texas at Austin combines a numerical implementation of the Pennes equation of bioheat transfer with the precise timing and orchestration of the problems of calibration, optimal control, data transfer, registration, finite element mesh refinement, cellular damage prediction, and laser control. The ultimate goal of this research is to provide the medical community a predictive computational tool that may be used by a surgeon during a minimally invasive hyper- or hypothermia treatment of a cancer-infected tissue. The tool controls the thermal source, provides a prediction of the entire outcome of the treatment, and, using intraoperative data, updates itself to increase the accuracy of the prediction. A current working snapshot of the entire control system is provided within this chapter. Current results demonstrate the importance of modeling the heterogeneity within the patient-specific biological domain to the accuracy of the computational solution. Through inversion of the constitutive nonlinearities, results also reinforce the experimentally observed phenomena of decreased perfusion in the damage region and hyperperfusion surrounding the damage region.

Minimally invasive treatments of cancer are key to improving posttreatment quality of life. Thermal therapies delivered under various treatment modalities are a form of minimally invasive cancer treatment that has the potential to become an effective option to eradicate the disease, maintain the functionality of infected organs, and minimize complications and relapse. However, the ability to control the energy deposition to prevent damage to adjacent healthy tissue is a limiting factor in all forms of thermal therapies [1], including cryotherapy, microwave, radio frequency, ultrasound, and laser. The combination of image guidance with computational prediction has the potential to allow unprecedented control over the bioheat transfer. Image guidance facilitates real-time treatment monitoring through temperature feedback during treatment delivery [2,3], and high-performance numerical implementations of mathematical bioheat transfer models can use the current-time thermal-imaging data to predict the outcome of the treatment minutes in advance [4].

The cyberinfrastructure under development at the University of Texas at Austin is an example of a dynamic data-driven feedback control system wherein the digitized bioheat transfer models control the heat transfer while simultaneously

using real-time imaging data to update the accuracy of the prediction. The aim of the control system is to provide the medical community with a real-time computational tool for visualization of the predicted temperature and damage fields, allowing for patient-specific optimized therapy guidance. The current control system is applicable to tissues that are stationary during imaging and uses an interstitial laser fiber as the thermal source. The purpose of this chapter is to provide a working snapshot of the current cyberinfrastructure.

9.2 CONTROL SYSTEM IMPLEMENTATION

Figure 9.1 provides an outline of the data flow between the major software modules of the control system. Communication connecting the software modules at an actual laboratory at the M. D. Anderson Cancer Center in Houston, Texas, to the computing and visualization center in Austin, Texas, is currently handled via batch *secure file transfer protocol* (sftp) over a commercial GigE Internet connection. The Level Set Boundary-Interior-Exterior (LBIE) Mesher* generates a patient-specific finite element mesh of the biological domain using preoperative magnetic resonance imaging (MRI) data. Prior to treatment, the location of optical fiber and laser power are optimized to control heat shock protein (HSP) expression, eliminate and sensitize cancer cells, and minimize damage to healthy cells. During treatment, intraoperative MRI data are used to register the computational domain with the biological domain, and real-time thermal-imaging MR thermal imaging (MRTI) data drive the calibrations aligning the parameters of the bioheat transfer model to the patient's biological tissue values. As new thermal-imaging data are acquired intermittently, the computational prediction is compared to the measurements of the real-time thermal images and the differences seen are used to update the computations of the optimal laser parameters as well as goal-oriented mesh adaptation [5], where appropriate. The image acquisition by the computers in Austin implicitly controls the power wattage output of the laser in Houston. The software infrastructure is built from the Petsc [6] parallel computing paradigm and the Toolkit for Advanced Optimization (TAO; Argonne National Laboratory, Argonne, Illinois) [7] parallel optimization library. Advanced Visual Systems (AVS; Waltham, Massachusetts) [8] is used in conjunction with a virtual network computing (VNC) server for remote visualization. AVS coroutines are used to manage and coordinate the simultaneous visualization of the MRI anatomical image, the MRTI thermal image, and finite element data sets.

---

* Software available at http://cvcweb.ices.utexas.edu/cvc.
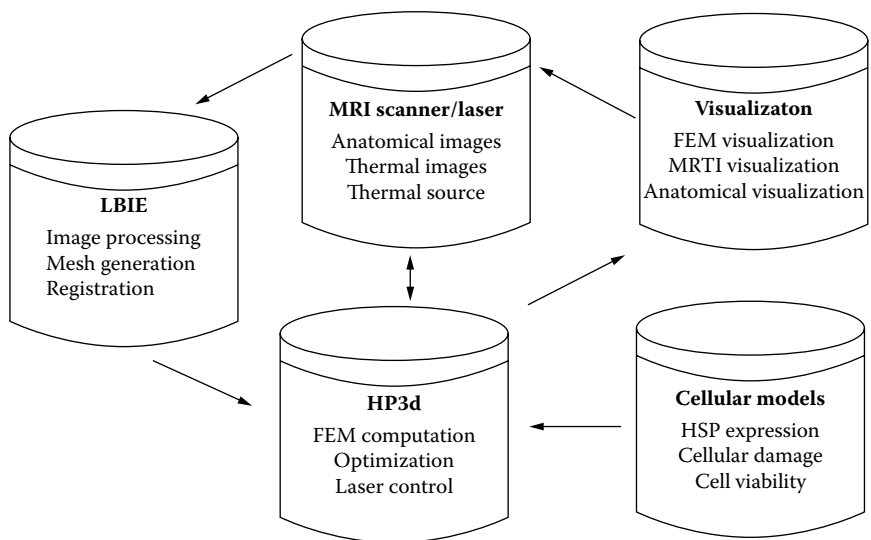
Figure 9.1 The computational infrastructure has five main modules: heating and imaging, finite element mesh generation, finite element computation, cellular damage models, and visualization. The data flow between the control system modules is illustrated.

A high-level abstraction of the HP3d* finite element solver is shown in Figure 9.2. The finite element solver is run at the Texas Advanced Computing Center (TACC), located in Austin. As illustrated in Figure 9.2, the problems of real-time calibration, optimal control, and goal-oriented error estimation are solved in parallel by separate groups of processors. Periodically during treatment, the groupwise optimization solutions and error estimates are collected on the control task. A skeleton of the entire finite element method (FEM) mesh of the biological domain is stored on the control task. Using the collective error estimates, a mesh refinement strategy is computed on the control task, and both the collective optimization solutions and refinement strategy are broadcast to the individual computational groups. The data server shown in Figure 9.2 reads in the thermal images from disk, filters the thermal images to remove noise, broadcasts the thermal images to each computational group as needed, and transmits the laser power to Houston. The timing of the laser power control is implicit through the image acquisition by the HP3d data server in Austin. As new thermal images are written to disk physically in Houston, they are transferred to disk at TACC. When the data server detects that the full set of thermal images for a time instance is available, the power to be used for the next time interval is sent to Houston.

* Software available at http://dddas.ices.utexas.edu.
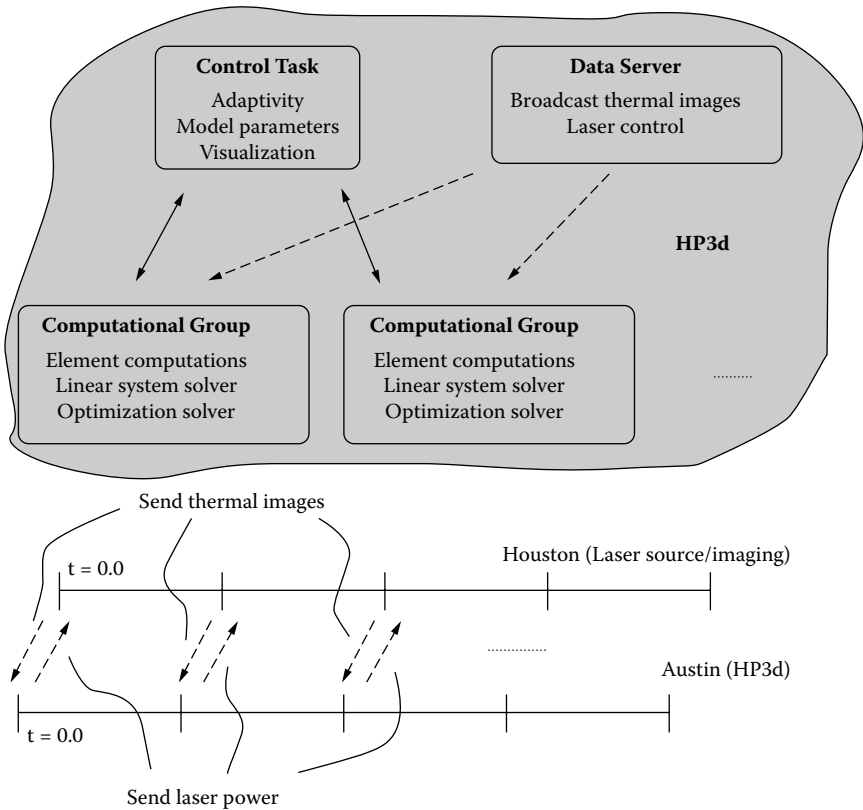
Figure 9.2   The finite element computations are performed on a parallel computing architecture using multiple groups of computed tasks to simultaneously solve disjoint numerical problems of the control system. A control task is used to gather and broadcast the individual solutions of the computational groups. A data server broadcasts filtered thermal images to individual computational groups as requested. The imaging implicitly controls the laser power output. As a new thermal image is acquired by HP3d in Austin, the power wattage for the next time interval is transmitted to the laser.

9.3   IMAGING TO FINITE ELEMENT MESH PIPELINE

The imaging-to-modeling software system for anatomical MRI data employs both image-processing and geometry-processing functionalities to produce a suitable linear or higher-order meshed model of the anatomy. Figure 9.3 describes the data flow layout. The major algorithmic components of each of the processing units is described in this section. The reader must note that the modules are selectively used depending on the nature and quality of the imaging data.

9.3.1   Image Processing

The input raw imaging data are often of poor quality, which makes it difficult to build a quality meshed model of the anatomy under investigation. In order to
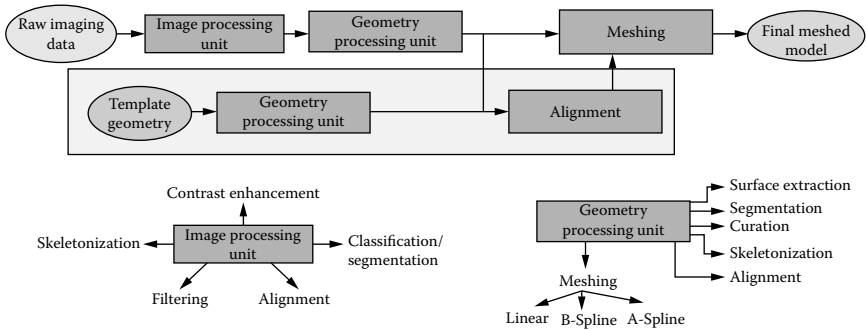
Figure 9.3 Data flow of imaging-to-meshing software system: There are two major processing units: image processing and geometry processing. The image-processing unit consists of modules for *contrast enhancement*, *classification and segmentation*, *filtering*, *skeletonization*, and *alignment*. The geometry-processing unit consists of *surface extraction*, *curation*, *segmentation*, *skeletonization*, *alignment*, and *meshing*; meshing is further subdivided into linear and higher-order boundary element and finite element mesh generation components. The three-dimensional (3D) anatomical magnetic resonance imaging (MRI) data are first passed through the image-processing unit for improvement of image quality, and are then processed by the geometry-processing unit for extraction of a clean geometry annotated with the present features. Finally, the clean geometry is converted to a linear or higher-order mesh. Occasionally, to deal with incomplete or low-quality imaging data, a twin data-processing pipeline is employed where a template geometry is processed to extract vital geometric information.

improve the image quality, we have developed a suite of image-processing functionalities that facilitate further processing. The modules encapsulated in the image-processing units are as follows:

1. *Contrast enhancement*: Improves the contrast of the image to help extraction of the domain of interest [9].
2. *Filtering*: Removes the noise by modifying the input image using bilateral filtering coupled with an anisotropic geometric diffusion **partial differential equation (**PDE) [10].

$$\partial_t \phi - \|\nabla\phi\| \, div\left(D^\sigma \frac{\nabla\phi}{\|\nabla\phi\|} \right) = 0$$

3. *Segmentation*: Segments an image into anatomically separate regions of interest using a fast marching method [11]; each region can then be extracted from the raw image [12].
4. *Image skeletonization*: Extracts lower-dimensional features from the image by analyzing the critical points of the imaging data [13,14].

5. *Flexible alignment*: Performs affine transformation to best fit an image of a biological system onto a different instance of the same [15].

9.3.2 Geometry Processing

After passing the input raw image through the modules of the image-processing unit, an improved image is obtained on which the geometry-processing routines are applied. The modules encapsulated in this unit are dedicated to better understanding the features of the model in order to improve the topological and geometric qualities that help in producing a correct meshed model of the domains of interest.

1. *Surface extraction*: Geometry extraction from the imaging data is done either by using contouring [16,17] or by reconstructing a piecewise triangulated or higher-order surface model from the boundary voxels of the segmented regions [18–20].

2. *Curation and filtering*: The initial surface model extracted from the imaging data has topological anomalies, namely, small components, spurious noisy features, and the like. The algorithms developed to cure the model of such anomalies include point cloud regularization [21], and volumetric primal and dual space feature quantification [22,23].

3. *Segmentation*: Geometric segmentation of an initial model often leads to better understanding of the quality of the model in terms of its topology N-d geometry. We have developed a geometry segmentation module based on the distance function induced by the geometry under investigation [22].

4. *Skeletonization*: The skeletal feature of a model provides a lower-dimensional description of a geometry that is helpful in building further meshed models of the anatomy, as was utilized in Zhang et al. [24]. We have developed a skeletonization algorithm that extracts a polylinear or polygonal skeletal structure from the geometric model [25] and further helps in annotating the shape into tubular or flat regions.

5. *Meshing*: The task of meshing is primarily divided into two parts—boundary element and finite element meshing. Each part has three subparts depending on if the resulting mesh is linear or higher order. For boundary element meshing, we have three options, namely, triangle or quadrilateral meshing [26], B-spline meshing, and A-spline meshing [27]. Similarly, for finite element meshing, we also have developed three different meshing modules, namely, tetrahedral or hexahedral meshing [26,28], solid nonuniform rational B-spline (NURBS) meshing [24], and A-spline meshing [29].

9.4 GOVERNING EQUATIONS

The governing state equations of the control system are built around the Pennes bioheat transfer model.

Find the spatially and temporally varying temperature field $u(\beta,\mathbf{x},t)$ such that

$$\rho c_p \frac{\partial u}{\partial t} - \nabla \cdot (k(u,\mathbf{x},\beta)\nabla u) + \omega(u,\mathbf{x},\beta)c_{blood}(u-u_a) = Q_{laser}(\beta,\mathbf{x},t) \quad \text{in } \Omega$$

given the Cauchy and Neumann boundary conditions

$$-k(u,\mathbf{x},\beta)\nabla u \cdot \mathbf{n} = h(u - u_\infty) \qquad \text{on } \partial\Omega_C$$

$$-k(u,\mathbf{x},\beta)\nabla u \cdot \mathbf{n} = \mathcal{G} \qquad \text{on } \partial\Omega_N$$

and the initial condition

$$u(\mathbf{x},0) = u^0 \qquad \text{in } \Omega$$

where c_p and c_{blood} are the specific heats of the tissue and blood, respectively; u_a is the arterial temperature; ρ is the density of the tissue; and h is the coefficient of cooling. The constitutive equations for the thermal conductivity, $k[\frac{J}{s \cdot m \cdot K}]$, and blood perfusion, $\omega[\frac{kg}{s \, m^3}]$, assume a nonlinear form, as shown in Figure 9.4.

$$k(u,\mathbf{x},\beta) = k_0(\mathbf{x}) + k_1 \, \mathrm{atan}(\tilde{k}_2(u - \hat{k}_3))$$

$$\omega(u,\mathbf{x},\beta) = \omega_0(\mathbf{x}) + \omega_1 \, \mathrm{atan}(\tilde{\omega}_2(u - \hat{\omega}_3))$$

Note that $\omega_0(\mathbf{x})$ is allowed to vary over the spatial dimension, as the blood perfusion within the necrotic core of a cancerous tumor or within a damaged tissue is expected to be significantly lower than that within the surrounding healthy tissue. $k_0(\mathbf{x})$ is also allowed to vary over the spatial dimension to capture the biological tissue heterogeneity. The isotropic laser source term, Q_{laser}, is of the form

$$Q_{laser}(\beta,\mathbf{x},t) = 3P(t)\mu_a\mu_{tr}\frac{\exp(-\mu_{eff}\|\mathbf{x}-\mathbf{x}_0\|)}{4\pi\|\mathbf{x}-\mathbf{x}_0\|} \qquad \begin{aligned}\mu_{tr} &= \mu_a + \mu_s(1-g)\\ \mu_{eff} &= \sqrt{3\mu_a\mu_{tr}}\end{aligned}$$

where μ_a and μ_s are laser coefficients related to laser wavelength and give the probability of tissue absorption and scattering of photons, respectively. $P(t)$ is the laser power wattage as a function of time. For the defined bioheat transfer model, let β denote all the model parameters:

$$\beta \equiv (k_0(\mathbf{x}),k_1,\tilde{k}_3,\hat{k}_3,\omega_0(\mathbf{x}),\omega_1,\tilde{\omega}_3,\hat{\omega}_3,P(t),\mu_a,\mu_s,\mathbf{x}_0)$$
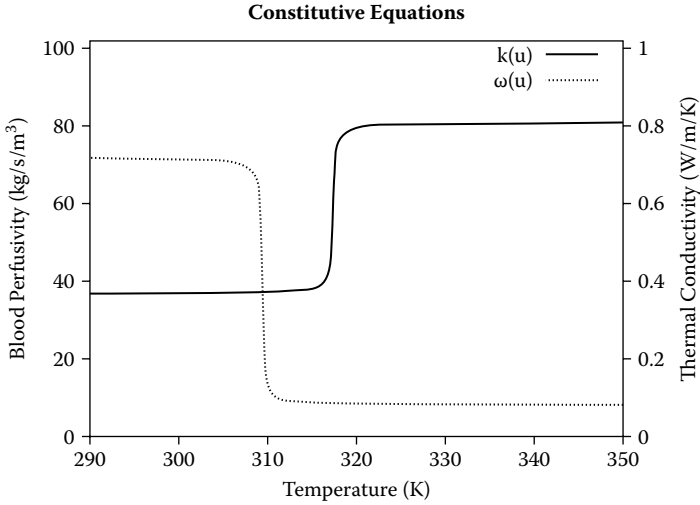
Figure 9.4 The temperature dependence of the blood perfusion and thermal conductivity material data used in the Pennes model are plotted against the left axis and right axis, respectively. The values shown were computed using inverse techniques applied to thermal imaging.

The variational form of the Pennes equation is given below:

$$C(u,\beta;v) = 0 = \int_0^T \int_\Omega \rho c_p \frac{\partial u}{\partial t} v + k(u,\mathbf{x},\beta) \nabla u \cdot \nabla v \, dxdt$$

$$+ \int_0^T \int_\Omega \omega(u,\mathbf{x},\beta) c_{blood}(u-u_a) v \, dxdt + \int_0^T \int_{\partial\Omega_N} G \, v \, dAdt \qquad (9.1)$$

$$- \int_0^T \int_\Omega Q_{laser}(\beta,\mathbf{x},t) v \, dxdt + \int_0^T \int_{\partial\Omega_C} h(u-u_\infty) v \, dxdt$$

The test function is denoted $v(\mathbf{x},t)$. Notice that each of the above integrals is well defined given that the thermal conductivity $k(u,\mathbf{x},\beta)$ and the perfusion $\omega(u,\mathbf{x},\beta)$ are bounded and assuming that $\frac{\partial u}{\partial t} \in L^2(\Omega)$.

The goal of the temperature-based optimal control and calibration problems within the control loop is to find the set of model parameters that minimize the space–time norm of the difference between the computed temperature field $u(\beta,\mathbf{x},t)$ and an ideal field $u^{ideal}(\mathbf{x},t)$. The mathematical structure is formally stated as follows.

Find the model coefficients, $\beta^* \in \mathbb{P}$, that produce the temperature field, $u^* \in \mathcal{V}$, such that

$$Q(u^*(\beta^*),\beta^*) = \frac{1}{2} \int_0^T \int_\Omega \chi(\mathbf{x})(u^*(\beta,\mathbf{x},t) - u_{ideal}(\mathbf{x},t))^2 \, dxdt + \Phi(\beta)$$

satisfies

$$Q(u^*(\beta^*),\beta^*) = \inf_{\beta \in \mathbb{P}} Q(u(\beta),\beta)$$

$$\mathbb{P} = \{\beta : \exists! u \text{ s.t. } C(u,\beta;v) = 0 \qquad \forall v \in \mathcal{V}\}$$

(9.2)

The ideal field for the calibration problem is the experimentally determined temperature field $u_{exp}(\mathbf{x},t)$. The ideal field for temperature-based optimal control is given as follows:

$$u^{ideal} = \begin{cases} 37.0°C & \mathbf{x} \in \Omega_H \\ 50.0°C & \mathbf{x} \in \Omega_C \end{cases}$$

The function $\Phi(\beta)$ is a penalty term added to the objective function used to keep the model parameters within physically acceptable bounds.

$$\Phi(\beta) = \sum_{i=1}^{N_{params}} \exp\left(\gamma \frac{\beta_i - \beta_i^{UB}}{\beta_i^{UB} - \beta_i^{LB}} \right) + \exp\left(-\gamma \frac{\beta_i - \beta_i^{LB}}{\beta_i^{UB} - \beta_i^{LB}} \right)$$

The dimension of the parameter space is denoted N_{params}. β_i denotes a particular parameter. The physically acceptable lower and upper bounds of the parameter, β_i, are denoted by β_i^{LB} and β_i^{UB}, respectively. The penalty term is scaled by $\gamma = 1000.0$.

9.4.1 Discretization of Equations

The optimization problem in Equation (9.2) is solved using an adjoint method to compute the gradient of the quantity of interest. The following Galerkin representation of the temperature field and adjoint variable is assumed:

$$u(\mathbf{x},t) = \sum_{k=1}^{N_{step}} \sum_{j=1}^{N_{dof}} \alpha_j^k(t)\phi_j(\mathbf{x}) \qquad p(\mathbf{x},t) = \sum_{k=1}^{N_{step}} \sum_{i=1}^{N_{dof}} \lambda_i^k(t)\phi_i(\mathbf{x})$$

where N_{step} is the number of time steps, N_{dof} is the number of Galerkin coefficients, and ϕ_i's are the finite element shape functions of polynomial order $p = 1,2,3\ldots$

$$\alpha_j^k(t) = \begin{cases} \dfrac{t_k - t}{t_k - t_{k-1}}\alpha_j^{k-1} + \dfrac{t - t_{k-1}}{t_k - t_{k-1}}\alpha_j^k, t \in [t_{k-1},t_k) \\ 0, \qquad\qquad \text{otherwise} \end{cases} \qquad \lambda_i^k(t) = \begin{cases} \lambda_i^k, t \in [t_{k-1},t_k) \\ 0, \text{ otherwise} \end{cases}$$

The time discretization of the power is assumed to be piecewise constant in time.

$$P(t) = \begin{cases} P_k, & t \in [t_{k-1}, t_k) \\ 0, & \text{otherwise} \end{cases}$$

The spatial variation of the parameter fields is assumed to have the following Galerkin representation:

$$k_0(\mathbf{x}) = \sum_j k_0^j \psi^j(\mathbf{x})$$

$$\omega_0(\mathbf{x}) = \sum_j \omega_0^j \psi^j(\mathbf{x})$$

where $\Psi(\mathbf{x})$ are piecewise constant across elements.

9.4.1.1 Time Stepping

Assuming that the test function is piecewise constant in time,

$$v(\mathbf{x},t) = \sum_{k=1}^{N_{step}} \sum_{i=1}^{N_{dof}} v_i^k(t)\phi_i(\mathbf{x}) \qquad v_i^k(t) = \begin{cases} v_i^k, & t \in [t_{k-1}, t_k) \\ 0, & \text{otherwise} \end{cases}$$

The governing equations (Equation 9.1) are solved with the following Crank-Nicolson time-stepping scheme.

$$\Delta t_k \int_\Omega \rho c_p \frac{u_k - u_{k-1}}{\Delta t_k} v_k + k(u_{k-\frac{1}{2}}, \mathbf{x}, \beta) \nabla u_{k-\frac{1}{2}} \cdot \nabla v_k \, dx$$

$$+ \Delta t_k \int_\Omega \omega(u_{k-\frac{1}{2}}, \mathbf{x}, \beta) c_{blood}(u_{k-\frac{1}{2}} - u_a) v_k \, dx$$

$$+ \Delta t_k \int_{\partial\Omega_C} h(u_{k-\frac{1}{2}} - u_\infty) v_k \, dA = \Delta t_k \int_\Omega Q_{laser}(\beta, \mathbf{x}, t_{k-\frac{1}{2}}) v_k \, dx \qquad (9.3)$$

$$- \int_{t_{k-1}}^{t_k} \int_{\partial\Omega_N} g v_k \, dA \quad \forall v_k \quad k = 1, 2, \ldots, N_{step}$$

where (using Einstein summation notation)

$$u_k = \alpha_j^k \phi_j(\mathbf{x}) \qquad u_{k-\frac{1}{2}} = \frac{\alpha_j^{k-1} + \alpha_j^k}{2} \phi_j(\mathbf{x}) \qquad v_k = v_i^k \phi_i(\mathbf{x})$$

The discretization (Equation 9.3) is of the form

$$\text{find } \vec{\alpha}^k = \left(\alpha_1^k, \alpha_2^k, \dots\right) \text{ s.t.}$$

$$\vec{f}(\vec{\alpha}^k) = \vec{0}$$

The Jacobian of this system of equations is

$$\frac{\partial f_i}{\partial \alpha_j^k} = \Delta t_k \int_\Omega \frac{\rho c_p}{\Delta t_k} \phi_j \phi_i \, dx + \Delta t_k \frac{1}{2} \int_{\partial \Omega_C} h \phi_j \, \phi_i \, dA$$

$$+ \Delta t_k \frac{1}{2} \int_\Omega \left(\frac{\partial k}{\partial u} \left(u_{k-\frac{1}{2}}, \mathbf{x}, \beta \right) \nabla u_{k-\frac{1}{2}} \phi_j + k \left(u_{k-\frac{1}{2}}, \mathbf{x}, \beta \right) \nabla \phi_j \right) \cdot \nabla \phi_i \, dx$$

$$+ \Delta t_k \frac{1}{2} \int_\Omega c_{blood} \left(\frac{\partial \omega}{\partial u} \left(u_{k-\frac{1}{2}}, \mathbf{x}, \beta \right) \left[u_{k-\frac{1}{2}} - u_a \right] + \omega \left(u_{k-\frac{1}{2}}, \mathbf{x}, \beta \right) \right) \phi_j \, \phi_i \, dx$$

9.4.1.2 Adjoint Gradient

The Adjoint Gradient of the quantity of interest is constructed from the derivative of the discretized equations with respect to a single model variable. The chain rule is used to compute the gradient of the quantity of interest for the optimization. The initial condition does not depend on the model parameters, $\frac{\partial u_0}{\partial \beta_i} = 0$.

$$\frac{\partial}{\partial \beta_i} Q(u(\beta, \mathbf{x}, t), \beta) = \sum_{k=1}^{N_{step}} \frac{\partial Q}{\partial u_k} \frac{\partial u_k}{\partial \beta_i} + \frac{\partial}{\partial \beta_i} \Phi(\beta)$$

The same Galerkin representation is used for u^{ideal} as u.

$$Q(u(\beta), \beta) = \frac{1}{2} \int_0^T \int_\Omega \rho c_p \chi(\mathbf{x}) (u(\beta, \mathbf{x}, t) - u^{ideal}(\mathbf{x}, t))^2 \, dx dt + \Phi(\beta)$$

$$= \frac{1}{2} \sum_{k=1}^{N_{step}} \int_{t_{k-1}}^{t_k} \int_\Omega \rho c_p \chi(\mathbf{x}) (u(\beta, \mathbf{x}, t) - u^{ideal}(\mathbf{x}, t))^2 \, dx dt + \Phi(\beta)$$

$$= \frac{\Delta t_k}{6} \sum_{k=1}^{N_{step}} \int_\Omega \rho c_p \chi(\mathbf{x}) \begin{pmatrix} u_{k-1}^2 - 2u_{k-1}u_{k-1}^{ideal} + u_{k-1}u_k \\[4pt] -u_{k-1}u^{ideal} + \left(u_{k-1}^{ideal} \right)^2 \\[4pt] -u_{k-1}^{ideal} u_k + u_{k-1}^{ideal} u_k^{ideal} + u_k^2 \\[4pt] -2u_k u_k^{ideal} + \left(u_k^{ideal} \right)^2 \end{pmatrix} + \Phi(\beta)$$

Derivatives are taken with respect to the numerically computed quantity of interest.

$$\frac{\partial Q(u,\beta)}{\partial \beta_i} = \sum_{k=1}^{N_{step}} \int_{t_{k-1}}^{t_k} \int_\Omega \rho c_p \chi(\mathbf{x})(u(\beta,\mathbf{x},t) - u^{ideal}(\mathbf{x},t)) \frac{\partial u}{\partial \beta_i} \, dx dt + \frac{\partial}{\partial \beta_i} \Phi(\beta)$$

$$= \sum_{k=1}^{N_{step}} \Delta t_k \int_\Omega \rho c_p \chi(\mathbf{x}) \left(\begin{matrix} \left[\frac{(u_{k-1} - u_{k-1}^{ideal})}{3} + \frac{(u_k - u_k^{ideal})}{6} \right] \frac{\partial u_{k-1}}{\partial \beta_i} \\ + \left[\frac{(u_{k-1} - u_{k-1}^{ideal})}{6} + \frac{(u_k - u_k^{ideal})}{3} \right] \frac{\partial u_k}{\partial \beta_i} \end{matrix} \right) dx$$

$$+ \frac{\gamma}{\beta_i^{UB} - \beta_i^{LB}} \left[\exp\left(\gamma \frac{\beta_i - \beta_i^{UB}}{\beta_i^{UB} - \beta_i^{LB}} \right) - \exp\left(-\gamma \frac{\beta_i - \beta_i^{LB}}{\beta_i^{UB} - \beta_i^{LB}} \right) \right]$$

The derivative of the discretized state (Equation 9.3) with respect to a single model variable yields the following:

$$\frac{\partial}{\partial \beta_i} C(u,\beta,v) = \Delta t_k \int_\Omega \frac{\rho c_p}{\Delta t_k} \left(\frac{\partial u_k}{\partial \beta} - \frac{\partial u_{k-1}}{\partial \beta} \right) v_k \, dx$$

$$+ \Delta t_k \int_\Omega \frac{\partial k}{\partial u}\left(u_{k-\frac{1}{2}}, \mathbf{x}, \beta\right) \frac{1}{2} \left[\frac{\partial u_{k-1}}{\partial \beta} + \frac{\partial u_k}{\partial \beta} \right] \nabla u_{k-\frac{1}{2}} \cdot \nabla v_k \, dx$$

$$+ \Delta t_k \int_\Omega k\left(u_{k-\frac{1}{2}}, \mathbf{x}, \beta\right) \frac{1}{2} \left[\nabla \frac{\partial u_{k-1}}{\partial \beta} + \nabla \frac{\partial u_k}{\partial \beta} \right] \cdot \nabla v_k \, dx$$

$$+ \Delta t_k \int_\Omega \frac{\partial \omega}{\partial u}\left(u_{k-\frac{1}{2}}, \mathbf{x}, \beta\right) \frac{c_{blood}}{2} \left[\frac{\partial u_{k-1}}{\partial \beta} + \frac{\partial u_k}{\partial \beta} \right] \left(u_{k-\frac{1}{2}} - u_a\right) v_k \, dx$$

$$+ \Delta t_k \int_\Omega \omega\left(u_{k-\frac{1}{2}}, \mathbf{x}, \beta\right) \frac{c_{blood}}{2} \left[\frac{\partial u_{k-1}}{\partial \beta} + \frac{\partial u_k}{\partial \beta} \right] v_k \, dx$$

$$+ \Delta t_k \int_{\partial \Omega_C} \frac{h}{2} \left[\frac{\partial u_{k-1}}{\partial \beta} + \frac{\partial u_k}{\partial \beta} \right] v_k \, dA$$

$$+ \Delta t_k \int_\Omega \frac{\partial k}{\partial \beta}\left(u_{k-\frac{1}{2}}, \mathbf{x}, \beta\right) \nabla u_{k-\frac{1}{2}} \cdot \nabla v_k \, dx$$

$$+ \Delta t_k \int_\Omega c_{blood} \frac{\partial \omega}{\partial \beta}\left(u_{k-\frac{1}{2}}, \mathbf{x}, \beta\right) \left(u_{k-\frac{1}{2}} - u_a\right) v_k \, dx$$

$$- \Delta t_k \int_\Omega \frac{\partial Q_{laser}}{\partial \beta}(\beta, \mathbf{x}, t_k) v_k \, dx = 0 \qquad k = 1, 2, \ldots, N_{step}$$

Solving for the adjoint variable, P_k, such that

$$\Delta t_k \int_\Omega \frac{\rho c_p}{\Delta t_k} \hat{u} p_k + \frac{1}{2} \frac{\partial k}{\partial u}\left(u_{k-\frac{1}{2}},\mathbf{x},\beta\right)\hat{u}\nabla u_{k-\frac{1}{2}} \cdot \nabla p_k \, dx$$

$$+\Delta t_k \int_\Omega \frac{1}{2} \frac{\partial \omega}{\partial u}\left(u_{k-\frac{1}{2}},\mathbf{x},\beta\right)\hat{u}\left(u_{k-\frac{1}{2}} - u_a\right) p_k \, dx$$

$$+\Delta t_k \int_\Omega \frac{1}{2} k\left(u_{k-\frac{1}{2}},\mathbf{x},\beta\right)\nabla\hat{u} \cdot \nabla p_k \, dx + \frac{1}{2}\omega\left(u_{k-\frac{1}{2}},\mathbf{x},\beta\right)\hat{u}p_k \, dx$$

$$+\Delta t_k \int_{\partial\Omega_C} \frac{h}{2} \hat{u}p_k \, dA = \Delta t_k \int_\Omega \rho c_p \chi(\mathbf{x})\left[\frac{\left(u_{k-1} - u_{k-1}^{ideal}\right)}{6} - \frac{\left(u_k - u_k^{ideal}\right)}{3}\right]\hat{u}$$

$$\forall \hat{u}, \qquad k = N_{step}$$

and

$$\Delta t_k \int_\Omega \frac{\rho c_p}{\Delta t_k} \hat{u} p_k + \frac{1}{2} \frac{\partial k}{\partial u}(u_{k-\frac{1}{2}},\mathbf{x},\beta)\hat{u}\nabla u_{k-\frac{1}{2}} \cdot \nabla p_k \, dx$$

$$+\Delta t_k \int_\Omega \frac{1}{2} \frac{\partial \omega}{\partial u}\left(u_{k-\frac{1}{2}},\mathbf{x},\beta\right)\hat{u}\left(u_{k-\frac{1}{2}} - u_a\right) p_k \, dx + \Delta t_k \int_{\partial\Omega_C} \frac{h}{2} \hat{u}p_k \, dA$$

$$+\Delta t_k \int_\Omega \frac{1}{2} k\left(u_{k-\frac{1}{2}},\mathbf{x},\beta\right)\nabla\hat{u} \cdot \nabla p_k \, dx + \frac{1}{2}\omega\left(u_{k-\frac{1}{2}},\mathbf{x},\beta\right)\hat{u}p_k \, dx$$

$$= \int_\Omega \rho c_p \chi(\mathbf{x})\Delta t_k\left[\frac{1}{6}\left(u_{k-1} - u_{k-1}^{ideal}\right) + \frac{1}{3}\left(u_k - u_k^{ideal}\right)\right]\hat{u}$$

$$+ \int_\Omega \rho c_p \chi(\mathbf{x})\Delta t_{k+1}\left[\frac{1}{3}\left(u_k - u_k^{ideal}\right) + \frac{1}{6}\left(u_{k+1} - u_{k+1}^{ideal}\right)\right]\hat{u} \, dx$$

$$- \begin{pmatrix} -\Delta t_{k+1} \int_\Omega \frac{\rho c_p}{\Delta t_{k+1}} \hat{u}p_{k+1} + \frac{1}{2} \frac{\partial k}{\partial u}\left(u_{k+\frac{1}{2}},\beta\right)\hat{u}\nabla u_{k+\frac{1}{2}} \cdot \nabla p_{k+1} \\[2mm] +\Delta t_{k+1} \int_\Omega \frac{1}{2} \frac{\partial \omega}{\partial u}(u_{k+\frac{1}{2}},\beta)\hat{u}\left(u_{k+\frac{1}{2}} - u_a\right) p_{k+1} \, dx \\[2mm] +\Delta t_{k+1} \int_\Omega \frac{1}{2} k\left(u_{k+\frac{1}{2}},\beta\right)\nabla\hat{u} \cdot \nabla p_{k+1} \, dx \\[2mm] +\Delta t_{k+1} \int_\Omega \frac{1}{2}\omega\left(u_{k+\frac{1}{2}},\beta\right)\hat{u}p_{k+1} \, dx + \Delta t_{k+1} \int_{\partial\Omega_C} \frac{h}{2} \hat{u}p_{k+1} \, dA \end{pmatrix}$$

$$\forall \hat{u}, \qquad k = N_{step} - 1, N_{step} - 2, \ldots, 1$$

implies that the numerical gradient of the quantity of interest may be computed as follows:

$$\frac{\partial Q(u,\beta)}{\partial \beta} = \sum_{k=1}^{N_{step}} \left(\begin{array}{l} -\Delta t_k \int_{\Omega} \frac{\partial k}{\partial \beta}(u_{k-\frac{1}{2}},\mathbf{x},\beta)\nabla u_{k-\frac{1}{2}}\cdot \nabla p_k\ dx \\[2ex] -\Delta t_k \int_{\Omega} c_{blood}\frac{\partial \omega}{\partial \beta}(u_{k-\frac{1}{2}},\mathbf{x},\beta)(u_{k-\frac{1}{2}}-u_a)p_k\ dx \\[2ex] +\Delta t_k \int_{\Omega} \frac{\partial Q_{laser}}{\partial \beta}(\beta,\mathbf{x},t_k)p_k\ dx \end{array} \right)$$

9.4.2 Calibration Results

The computational results presented in this section revisit the thermal-imaging data studied in Feng et al. [30] and Oden et al. [4]. The calibration algorithm presented in Section 9.4.1 is applied to these data sets to invert for the constitutive equation nonlinearities as well as the heterogeneity of the biological domain.

The effect of calibrating the nonlinear perfusion, $\omega(u,\mathbf{x},\beta)$, and the thermal conductivity, $k(u,\mathbf{x},\beta)$, parameters in the Pennes model was studied. Calibration was done with respect to MRTI thermal-imaging data of *in vivo* heating of canine brain tissue. The thermal-imaging data were acquired in the form of five two-dimensional (2D) 256×256 pixel images every 6 seconds for 120 time steps. The spacing between images was 3.5 mm. A manual craniotomy of a canine skull was performed to allow insertion of an interstitial laser fiber to provide the heating. A template base [32] finite element mesh was generated from 36 2D 256×256 pixel MRI images of the canine brain. The field view was 200 mm $\times$ 200 mm, with each image spaced 1 mm apart. The FEM prediction using *CRC Handbook* [31] linear material coefficients, $k(u,\mathbf{x},\beta)=0.527[\frac{W}{mK}]$ and $\omega(u,\mathbf{x},\beta)=6.0[\frac{kg}{sm^3}]$, is shown in Figure 9.5. Figure 9.6 shows the FEM prediction using calibrated nonlinear coefficients. A plot of the material coefficients obtained is shown in Figure 9.4. The data shown in Figures 9.5 and 9.6 illustrate a particular time instance. The upper-right windows in Figures 9.5 and 9.6 each show a cutline comparison of the filtered MRTI data with the unfiltered data. The upper-left windows in Figures 9.5 and 9.6 display an overlay of the MRTI thermal image onto the anatomical MRI image. The lower-left window in Figures 9.5 and 9.6 shows a 2D temperature slice through the 3D domain. The lower-right window is a cutline comparison of the filtered MRTI data to the FEM prediction. The accuracy of the predicted FEM solution shown in Figure 9.6 was obtained by inverting for the constitutive nonlinearities. The damage of the tissue is reflected in the decrease in perfusion for high temperatures within the damaged region and hyperperfusion surrounding the damaged region. As shown in Oden et al. [4],
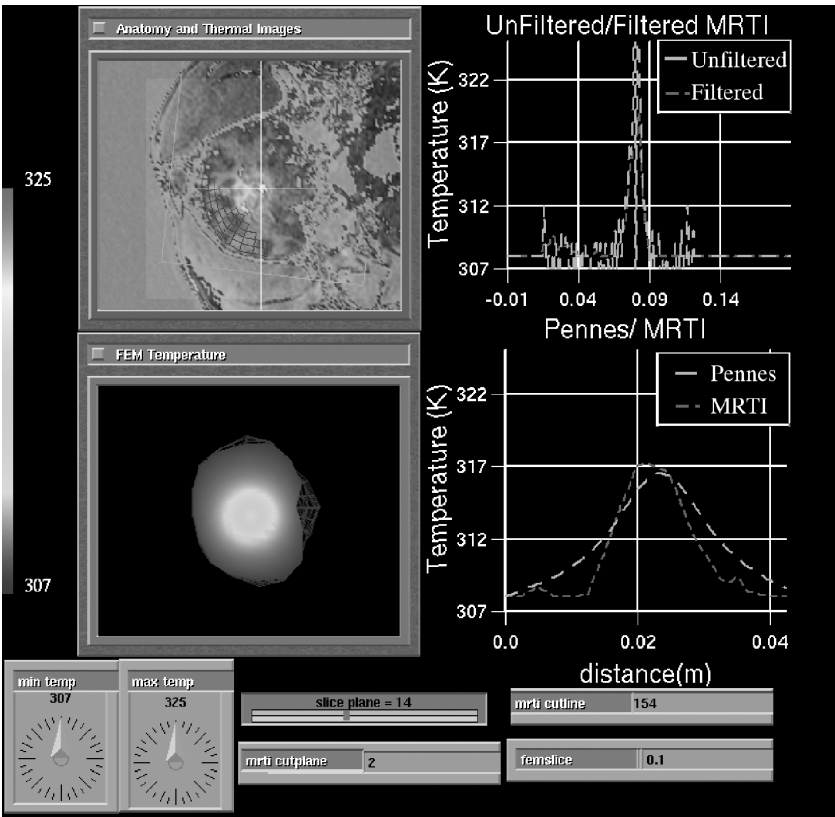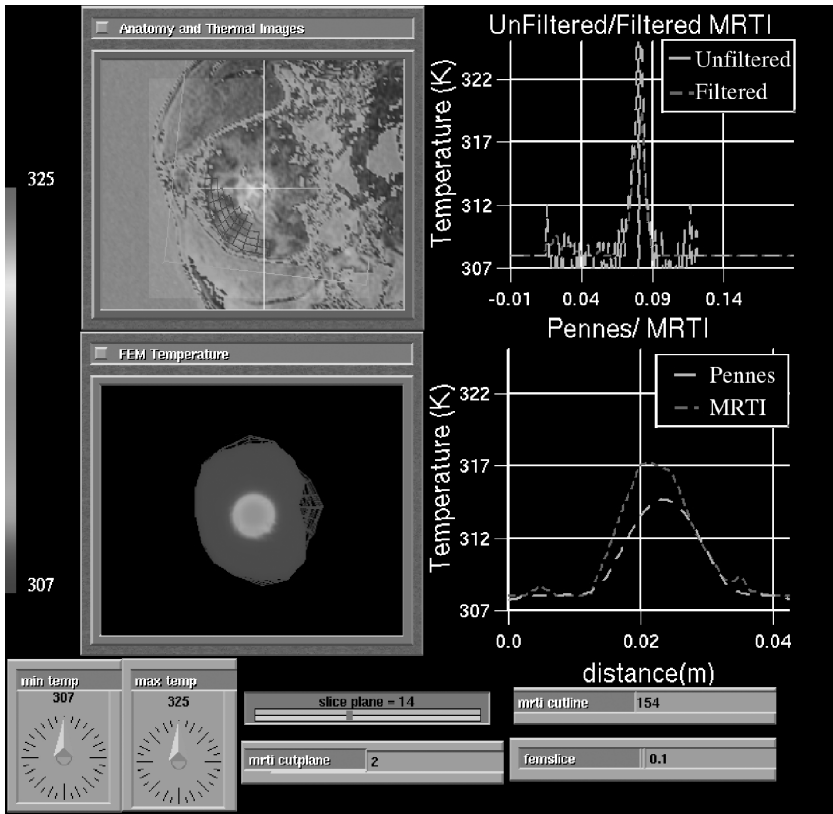
Figure 9.5 Thermal images of *in vivo* heating of a canine brain were taken every 6 seconds over a period of 12 minutes. The top left shows the anatomy with a particular time instance of the thermal images overlaid. The linear Pennes equation was solved using *CRC Handbook* [31] perfusion and thermal conductivity values for the canine brain, and the bottom left shows the linear finite element method (FEM) prediction at the same time instance for comparison. The temperature range shown is from 307 K to 325 K. The top right shows a cutline through the thermal image data. The unfiltered and filtered image data are plotted along the cutline. The bottom right compares the FEM predicted temperature and filtered thermal image along a cutline through the FEM mesh.

the linear case captures the early time heating well, but the cutlines in Figures 9.5 and 9.6 illustrate that the material nonlinearities are necessary to model the late time heat dissipation. The results presented in Figure 9.8 indicate that a spatially varying inversion for the perfusion field should provide a means to further increase the accuracy of the FEM temperature prediction of the canine brain data (Figure 9.6).

Allowing the perfusion and thermal conductivity model parameters to vary as a spatial field is seen to have a tremendous effect on the model calibrations. Inverting for the spatial variation in the parameters embeds the biological tissue
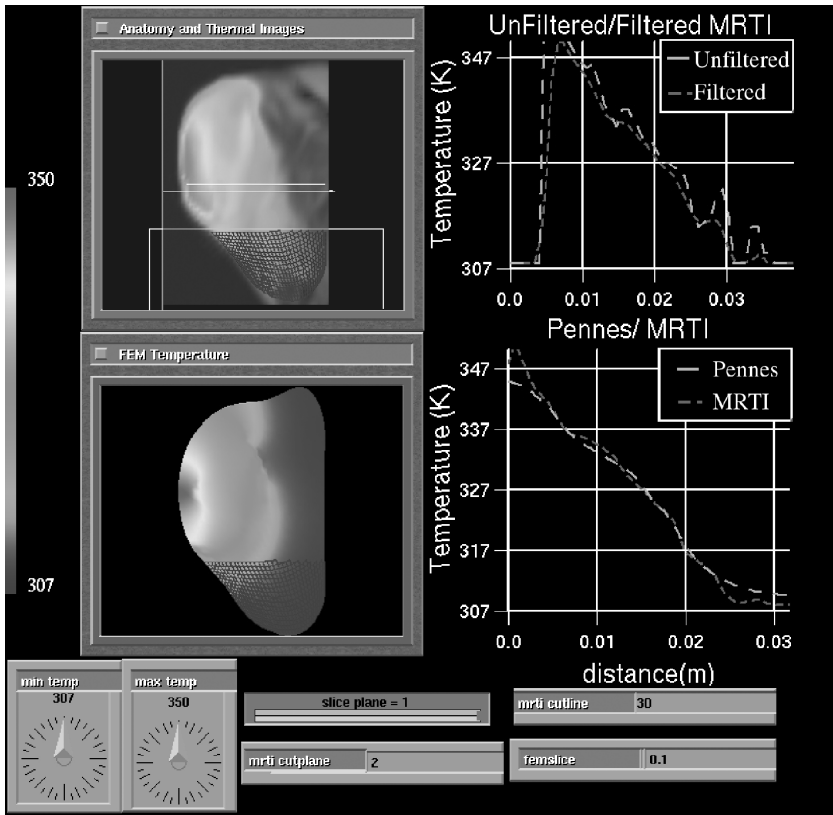
Figure 9.6 Thermal images of *in vivo* heating of a canine brain were taken every 6 seconds over a period of 12 minutes. The top left shows the anatomy with a particular time instance of the thermal images overlaid. The Pennes equation was solved with a set of nonlinear perfusion and thermal conductivity material coefficients that were calibrated to the thermal images, and the bottom left shows the nonlinear FEM prediction at the same time instance for comparison. The temperature range shown is from 307 K to 325 K. The top right shows a cutline through the thermal image data. The unfiltered and filtered image data are plotted along the cutline. The bottom right compares the FEM predicted temperature and filtered thermal image along a cutline through the FEM mesh.

heterogeneity within the Pennes model. Imaging data of an external laser applied to a tumor grown on a mouse's hind leg were used to study the effect of the parameter field inversion. Sixty thermal images were acquired at an interval of 5 seconds. A single time instance of the data is shown in Figures 9.7 and 9.8. The field of view is 4×6 cm^2, and the thickness associated with the MRI and MRTI images is 3 mm. Figures 9.7 and 9.8 compare the FEM prediction using textbook linear material coefficients to the calibrated heterogeneous material coefficients applied to the *in vivo* heating of a tumor grown on a mouse. The upper-right windows in Figures 9.7 and 9.8 each show a cutline comparison of the filtered MRTI
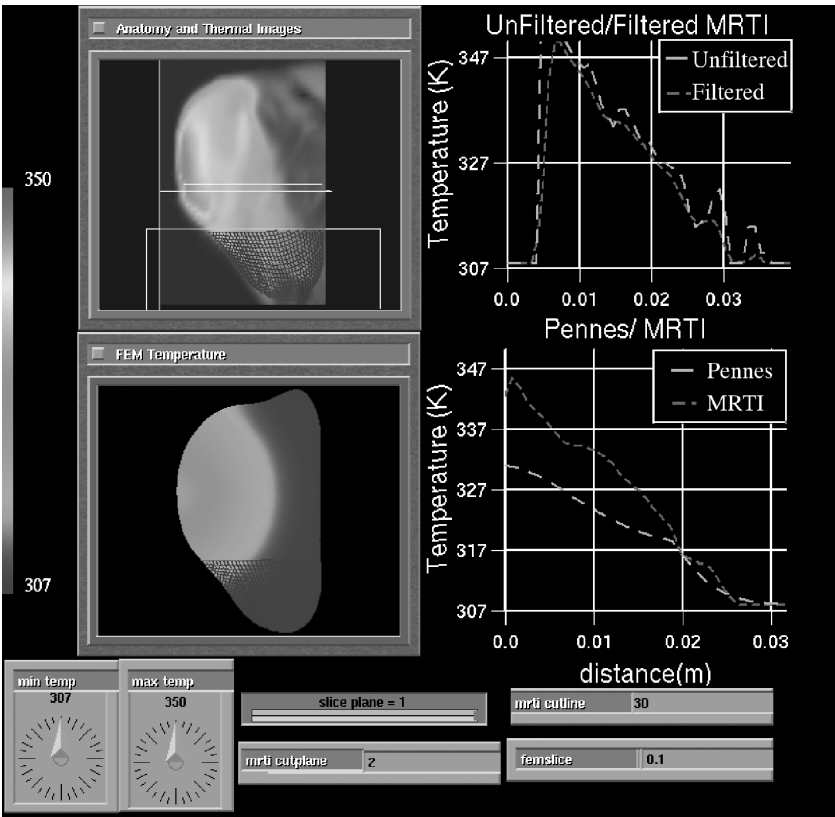
Figure 9.7   Thermal images of *in vivo* heating of a tumor grown on the hind leg of a mouse were taken every 5 seconds over a period of 5 minutes. The top left shows the anatomy with a particular time instance of the thermal images overlaid. The linear Pennes equation was solved using *CRC Handbook of Mechanical Engineering* [31] perfusion and thermal conductivity values for the tissue, and the bottom left shows the linear FEM prediction at the same time instance for comparison. The temperature range shown is from 307 K to 350 K. The top right shows a cutline through the thermal image data. The unfiltered and filtered image data are plotted along the cutline. The bottom right compares the FEM predicted temperature and filtered thermal image along a cutline through the FEM mesh.

data with the unfiltered data. The upper-left windows in Figures 9.7 and 9.8 display an overlay of the MRTI thermal image onto the anatomical MRI image. The images are 49 × 56 pixels. The lower-left window in Figures 9.7 and 9.8 shows a 2D temperature slice through the 3D domain. The lower-right window is a cutline comparison of the filtered MRTI data to the FEM prediction. The agreement between the predicted FEM solution and the MRTI thermal images shown in Figure 9.8 illustrates the importance of inverting for the field of material heterogeneity. Figure 9.8 represents a ≈4100 parameter optimization problem. Figure 9.9

Figure 9.8 Thermal images of *in vivo* heating of a tumor grown on the hind leg of a mouse were taken every 5 seconds over a period of 5 minutes. The top left shows the anatomy with a particular time instance of the thermal images overlaid. The Pennes equation was solved with a spatially varying field of perfusion and thermal conductivity material that were calibrated to the thermal images, and the bottom left shows the nonlinear FEM prediction at the same time instance for comparison. ≈4100 model parameters were optimized to recover the material heterogeneity. The temperature range shown is from 307 K to 350 K. The top right shows a cutline through the thermal image data. The unfiltered and filtered image data are plotted along the cutline. The bottom right compares the FEM predicted temperature and filtered thermal image along a cutline through the FEM mesh.

shows the optimizer evolution of the material heterogeneity inversion for the thermal conductivity fields and blood perfusion fields. The initial guess for the material coefficients was assumed homogeneous, and the optimizer determined a sufficient field variation of the parameters that allows the Pennes model to accurately predict the temperature field seen in the thermal images. The values of the thermal conductivity field found by the optimizer are above the physical range seen in the *CRC Handbook of Mechanical Engineering* [31]. Future work includes correlating the computed inverted parameter field with the physical tissue.
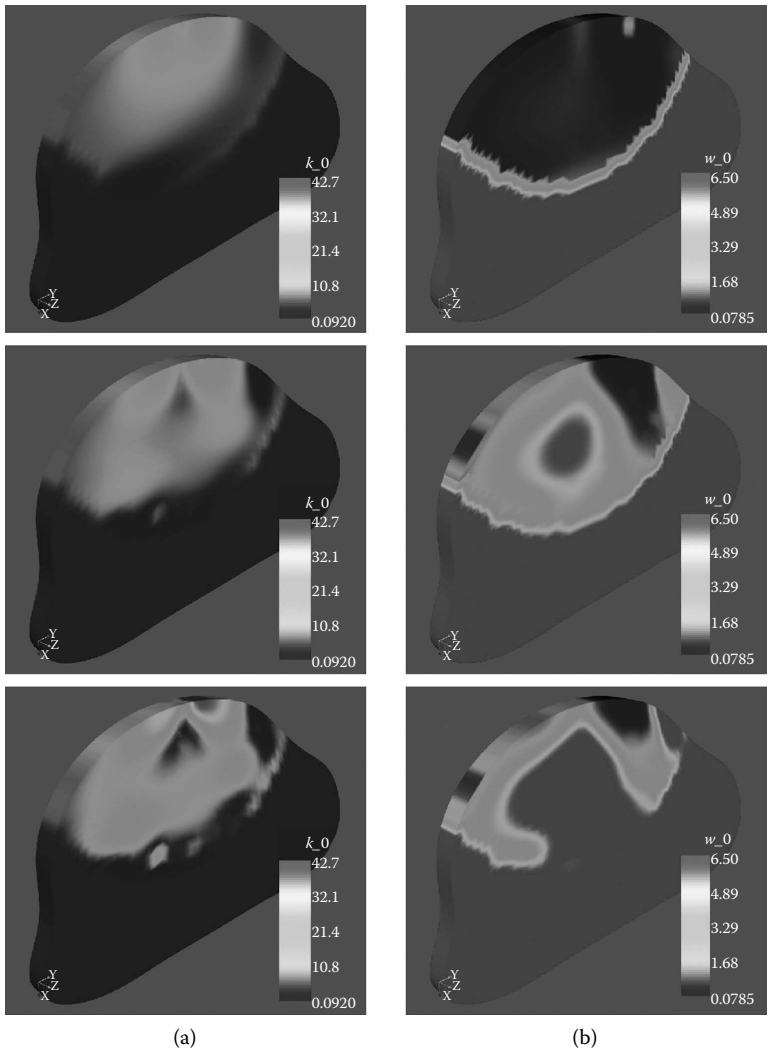
Figure 9.9   Thermal-imaging data were used to drive an inverse problem to recover the biological tissue heterogeneity. ≈ 4100 model parameters representing the blood perfusion and thermal conductivity fields of the biological domain were optimized to allow the Pennes model to accurately predict the temperature field seen in the thermal images. As shown at the top of the figure, the parameter fields are initially assumed homogeneous. The evolution of the optimizer's inversion for the parameter fields is shown. (a) and (b) show the evolution of the thermal conductivity and blood perfusion fields, respectively.

9.5   CELL STUDIES

Damage and heat shock protein (HSP) optimizations are based on *in vitro* cellular data. Due to the role of HSPs in posttraumatic cell survival, one needs to have proper data determining the changes in HSP expression induced by the thermal stress. HSPs are molecular chaperones responsible for protecting the cells from damage. They are normally present in both prokaryotic and eukaryotic cells in minimal quantities. Various stressful stimuli can lead to increased expression of HSPs, including, but not limited to, high or low temperature, acidosis, ischemia, hypoxia, and ultraviolet (UV) irradiation [33]. Denatured proteins, if bigger than 100 to 150 amino acids in size, cannot refold properly by themselves [34]. HSPs prevent improper aggregation of these damaged proteins and direct newly formed proteins for final packaging, degradation, and repair [35]. As mentioned earlier, exposure to sublethal stimuli would cause an increase in production of HSPs, which, in turn, would cause increased tolerance to further stress. This is a very important protection mechanism for cells [36]. Some members of the HSP family are inhibitors of apoptosis proteins. Therefore, an increase in expression of HSPs would lead to blocking pathways that lead to apoptosis. The prevention of apoptotic death of the damaged cells would increase cell survival rates [37]. In cancer treatment, it lowers the response of the cells to chemotherapeutic agents.

The goal of thermal therapy is to ablate malignant tissue while preserving normal tissue as much as possible. To make a correct estimate of damage in malignant and normal areas, one needs to have prior knowledge of the mechanics and kinetics of thermal damage in the appropriate cell types. This information can be acquired by conducting controlled stress experiments in model systems such as cell cultures. The subject culture can be obtained either from established cell lines or by establishing primary cultures from harvested tissue. These procedures are widely reported in the literature [38–40].

9.5.1   Heating Protocol

The heating experiments were done on primary cultures of prostate stromal cells isolated from canine prostate tissue following the protocol described by Srinivasan et al. [38]. Controlled thermal stress is applied to culture systems by immersing them in a heated liquid bath. The heating medium used in our experiments contains no L-glutamine, to prevent cellular damage due to production of ammonia secondary to breakage of L-glutamine. The heating is done in a water bath for only one culture flask at each given time to prevent a drop in temperature of the bath. In order to induce a sharp increase in the temperature of the samples, the heating medium is preheated to the same temperature as is desired for the heating experiment itself. The flasks are washed with 37°C PBS. Preheated medium is added to the flasks, which are submerged in a heated water bath for the desired duration of heating. Then the heating medium is replaced with 37°C growth medium, and

the flasks are returned to the 37°C incubator. Samples are checked for viability 60 hours postheating. At the end of this time, samples are trypsinized, and the cells are removed and washed in cold PBS twice and resuspended in binding buffer at 10 g/ml concentration. Annexin V and PI (BD Biosciences) (Franklin Lakes, New Jersey) are used to detect apoptotic and dead cells, respectively. The samples are analyzed using BD FACSCalibur (BD Biosciences). This flow cytometer is used primarily for cell analysis with simultaneous acquisition of forward scatter, side scatter, and fluorescence. On the forward-scattering (FS) versus side-scattering (SC) plot, the events with a low level of SC or FS are considered to be dead cells or debris from disintegrated cells. These events are later distinguished from each other using the fluorescence detected by FL 1 (filter 1 detects fluorescence emission centered at 530 nm; this would be able to detect the emission from Annexin V) and FL 2 (detects emission centered at 585 nm; this corresponds to emission from PI). On a dot plot of FL 1 versus FL 2, events negative for both are considered to be debris, whereas the events positive for either Annexin V or PI are counted as dead cells. Furthermore, on the FS versus SC plot, the events with a high level of SC and FS are considered to be live or dead cells, which later on would be distinguished from each other using the dot plot of FL 1 versus FL 2; events negative for both are considered to be live cells, and the events positive for either Annexin V or PI (or both) would be considered dead cells. Data analysis is performed using FlowJo 8.0 (BD Biosciences). HSP expression data presented here are based on the work done by Rylander et al. [35]. To determine the relationship between HSP expression and thermal stress, after heating the cell flasks by the method described above, cells lysed were in a buffer solution 16 to 18 hours postheating, and then the supernatant was analyzed using Western blotting. Later, a spectrophotometer at 595 nm (Beckman DU 530) (Beckman Coulter, Fullerton, California) and protein dye assay (Bio-Rad 500-0002) (Bio-Rad, Hercules, California) were used, and the relative concentration of HSP to actin in the cell lysate was measured.

9.5.2 Cell Study Results

Figure 9.10 shows the viability data for heating done at 45°C, 50°C, and 56°C for time durations of 5, 10, and 15 minutes. Cell viability is defined as the percentage of live cells in the cell culture flasks 60 hours after thermal stress. As expected, the higher the temperature and duration of heating, the lower the cell viability.

Rylander measurements for HSP70 (i.e., 70 kilodalton heat shock proteins) expression at different durations and temperatures are shown in Figure 9.11 [35]. As can be seen, the HSP expression increases for each given temperature up to a certain duration of heating, after which it drops sharply. Figure 9.12 shows Rylander et al. [35] cell viability data for different time durations and temperatures.

The goal of our experiments is to find the ideal duration and temperature that maximizes trauma in tumoral cells and minimizes damage in the normal region.
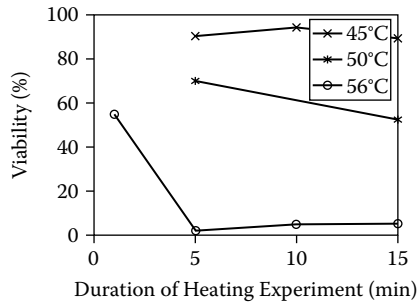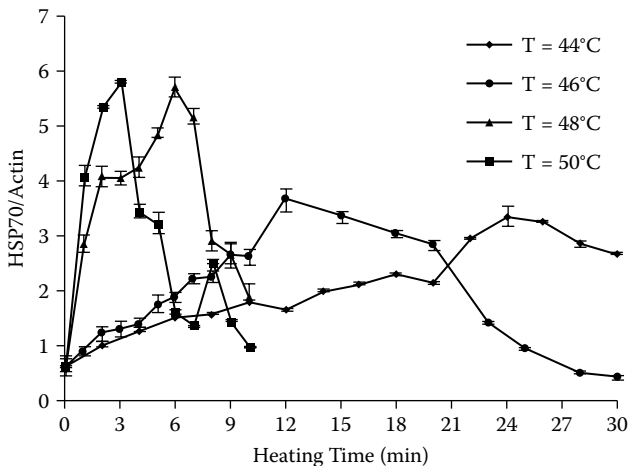
Figure 9.10   Cell viability as a function of heating time and temperature evaluated at 60 hours post-heating.

To study the effect of cell viability and HSP expression, Rylander et al. [41] have introduced a figure of merit (FOM), which is defined as follows:

$$\text{FOM} = \left(\frac{\text{cell viability}}{10} \right) \left(\frac{\left(\frac{\text{HSP70}}{\text{actin}} \right)_{sample}}{\left(\frac{\text{HSP70}}{\text{actin}} \right)_{control}} \right)$$

The FOM has its maximum value at 50°C and duration of 1 minute. This analysis provides an initial guide in the design of therapeutic protocols.

Figure 9.11   Normalized heat shock protein (HSP) and actin expression as a function of heating time and temperature evaluated at 16 to 18 hours postheating. The average error is ±0.13 mg/ml, $n = 3$ [35].
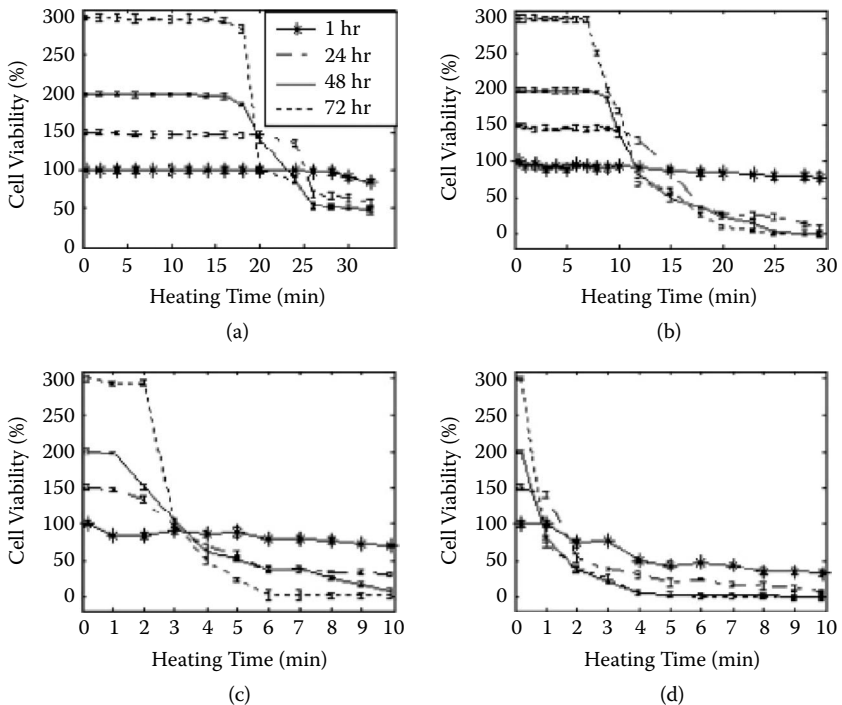
Figure 9.12   Cell viability following variable duration of thermal stress for temperatures of (a) 44°C, (b) 46°C, (c) 48°C, and (d) 50°C measured at t = 1, 24, 48, and 72 hours postheating. The average error is ±3%, and the number of samples = 3 [35].

9.6 CELL DAMAGE MODELS

Thermal damage processes in cells and tissues are usually quantified by kinetic models based on a first-order rate process to characterize pathological transformation to specific states by observable alterations such as coagulation or desiccation. While the Arrhenius law is commonly used to describe the rate of chemical reactions involving temperature [42,43], Henriques and Moritz were the first to propose a model of this form in 1947 to quantify thermal damage specifically for tissue [44,45]. The thermal injury associated with exposing cells to hyperthermia conditions is generally predicted using the Arrhenius law based on the assumption that the rate of cell damage is proportional to $\exp(-E_a/R_u)$, where E_a is the activation energy (or the heat of activation), R the universal gas constant, and u the temperature in degrees Kelvin [46], with a few exceptions (e.g., Roti Roti and Henle [47]).

Although thermal damage models based on the Arrhenius law are widely used, the model possesses some inherent limitations, which include its inability to predict cellular injury over a wide hyperthermic temperature range and

throughout the entire heating process, its sensitivity to small changes in parameters, and the ambiguity in interpretation of model parameters characterizing the cell damage formulation. In fact, several basic questions can be raised. How do cells essentially respond to temperature? Why does the rate of thermal damage follow the first-order unimolecular chemical reaction? What is the biophysical interpretation of both parameters in the Arrhenius model? Some answers related to these questions may be found in Lepock [48], Pearce and Thomsen [49], and Philibert [50]. However, further investigation is warranted due to the complexity of these questions.

Experimental data [41,51] suggest that there are at least two transitional temperatures ("break points") at 43°C and 52°C in the temperature range from 39°C to 60°C. A different injury mechanism may be initiated at each of these temperatures. At the cellular or subcellular level, the sigmoidal phenomenon observed in the cell viability profile could be related to the melting of oligomers that occurs in DNA molecules [52], or due to the damage of the lipid bilayer of cell membranes. Although phospholipids are the major components of the bilayer, it is worth noting that other lipid components in the bilayer such as dodecanoic and tetradecanoic acids have melting temperatures of 44.2°C and 53.9°C, respectively [53]. Cells initially exhibit resistance to the thermal damage due to the induction of heat shock proteins by sublethal temperatures as autoregulatory mechanisms. With increases in temperature or extended exposure times, the heat shock proteins that participate in the rescue process are denatured and rendered nonfunctional. This phenomenon can be observed in measured cell viability data in which the cell damage rate is initially slow, followed by an injury rate dominated by exponential decay [41].

Usually, the Arrhenius model permits fitting of data solely within the exponential decay region of the curve where cell viability is plummeting due to extensive injury, but is not able to accommodate the "shoulder region" characterized by sustained high cell viability encountered in the initial stages of the heating process for lower temperatures. Cells exposed to $u < 54$°C experience high viability initially for a range of exposure times until a threshold thermal dose is achieved to initiate cellular injury and a corresponding decline in cell viability. In general, although it depends on cell line and temperature, cell viability profiles in this temperature range initially exhibit a shoulder region where cell viability remains high until a threshold lethal thermal dose is achieved to initiate rapid declines in cell viability. The Arrhenius model is capable of predicting the complete injury phenomena for cells exposed to $u < 54$°C, where thermal dose is substantial at short exposure times, causing rapid declines in cell viability immediately following thermal stress. However, three sets of injury parameters are required for different temperature regimes ($u < 43$°C, 43°C $\leq u \leq 54$°C, and $u > 54$°C) in order to permit accurate fitting of cellular injury data for the entire range of temperatures.

An additional problem with the thermal damage model based on the Arrhenius model is its numerical sensitivity of model parameters to small changes in measurement data. As a result, therapeutic outcomes could be compromised if the treatment planning is based on such models.

To overcome the weaknesses of the Arrhenius model described above, other types of models have been proposed for thermal damage of cells and tissues. These include models that are derived using statistical methods [54], an enzyme denaturation approach [55], and widely used kinetic theory [51,56–59]. For a discussion of various cell damage models, He and Bischof [46] provide a comprehensive review. Most of these models, however, relate thermal damage to the rate process in such a way that the rate of change with respect to temperature and time are decoupled.

In a recent study [60], a two-state model of *in vitro* cell death due to thermal insult is derived based on simple arguments motivated by classical statistical thermodynamics. This model characterizes two populations of viable (live) and damaged (dead) cells, which leads to the damaged cell population of the form $C(u,t) = \exp(-\Delta G/ku)/(1+\exp(-\Delta G/ku))$ or, alternatively, $C(u, t) = \frac{1}{2} + \frac{1}{2}\tanh(-\Delta G/2ku)$, where k is the Boltzmann constant and ΔG is interpreted as a change in a functional analogous to a classical Gibbs free energy, depending on both temperature and exposure time. We postulate that ΔG *is a linear function of time and is inversely proportional to temperature*. To determine ΔG, we use cell viability data for human prostate cancerous (PC3) and normal (RWPE-1) cells to calibrate the two-state cell damage model derived in this study. Excellent agreement between experimental data and the derived model is obtained through least-squares regression. As compared to the Arrhenius model, the two-state model captures the damage process more accurately over a wide hyperthermic temperature range, including the beginning phase (the shoulder region) when cells are first exposed to the heat shock. Also, the model successfully characterizes the sigmoidal phenomenon of the cell response.

9.6.1 Two-State Cell Damage Model

Consider a cell population with two distinct states (i.e., a cell is either live or dead). We apply classical arguments of statistical thermodynamics to derive a two-state model for cell damage under hyperthermia conditions. In an *in vitro* system of the fixed population of total n cells, we assume that there are only two species of cells in this population: dead or dying cells (including apoptotic and necrotic cells), and live cells.

Based on the standard argument of statistical thermodynamics, the following results for a two-state population can be obtained [60]:

$$C(u,t) = \frac{e^{-\Delta G/ku}}{1+e^{-\Delta G/ku}} \quad \text{and} \quad D(u,t) = \frac{1}{1+e^{-\Delta G/ku}} \tag{9.4}$$

or, equivalently,

$$C(u,t) = \frac{1}{2} + \frac{1}{2}\tanh(-\Delta G/2ku) \tag{9.5}$$

$$D(u,t) = 1 - C(u,t) = \frac{1}{2} - \frac{1}{2}\tanh(-\Delta G/2ku) \tag{9.6}$$

where $C(u,t)$ is the cell viability function and $D(u,t)$ is the cell damage function. Inspired by statistical thermodynamics, we let $\Delta G = \Delta H - u\Delta S$ and postulate that ΔH is a constant and ΔS a linear function in time (i.e., $\Delta S = \alpha_o t + \beta_o$). The notions of ΔG, ΔH, and ΔS are chosen to mimic changes in Gibbs free energy, enthalpy, and entropy.

Based on the results in Equation (9.4), the cell viability function $C(u,t)$ can also be defined as a solution to the following system of partial differential equations:

$$\begin{cases} \dfrac{\partial C(u,t)}{\partial t} = \alpha \cdot \dfrac{C(u,t)}{1 + e^{-\Delta G/ku}} \\[4mm] \dfrac{\partial C(u,t)}{\partial u} = \dfrac{h}{u^2} \cdot \dfrac{C(u,t)}{1 + e^{-\Delta G/ku}} \end{cases} \tag{9.7}$$

where $h = \Delta H/k$, $\alpha = \alpha_o/k$, and $\beta = \beta_o/k$ are constants. If $e^{-\Delta G/ku}$ is very small, then $1 + e^{-\Delta G/ku} \approx 1$ and Equation (9.7) can be approximated by

$$\begin{cases} \dfrac{\partial C(u,t)}{\partial t} = \alpha \cdot C(u,t) & (9) \\[4mm] \dfrac{\partial C(u,t)}{\partial u} = h \cdot \dfrac{C(u,t)}{u^2} \end{cases} \tag{9.8}$$
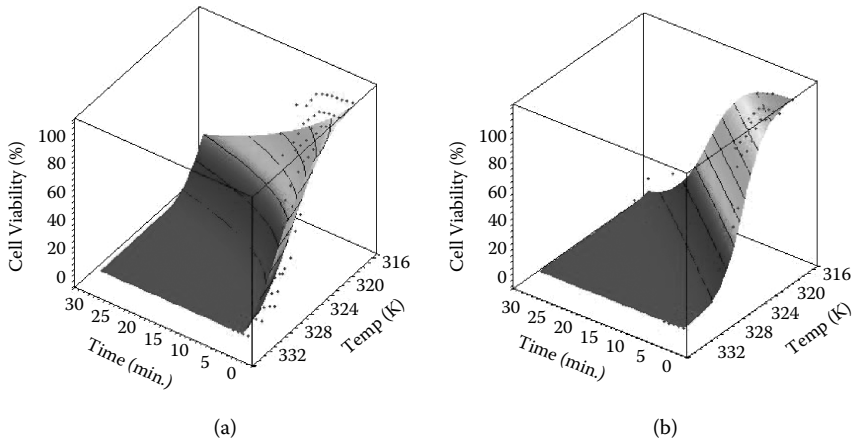
9.6.2 Parameter Estimation

To determine ΔG, we let $\Delta G = \Delta H - u\Delta S$ and $\Delta S = \alpha_o t + \beta_o$, where u and t are temperature and time, respectively, and ΔH, α_o, and β_o are constants. Then the first equation in Equation (9.7) can be converted to

$$\frac{\Delta G}{ku} = \frac{\Delta H - u\Delta S}{ku} = \ln\left(\frac{1 - C(u,t)}{C(u,t)}\right) \tag{9.9}$$

In other words,

$$\frac{\Delta H}{ku} - \frac{\Delta S}{k} = \left(\frac{\Delta H}{k}\right)\frac{1}{u} - \left(\frac{\alpha_o}{k}\right)t - \frac{\beta_o}{k} = \ln\left(\frac{1 - C(u,t)}{C(u,t)}\right) \tag{9.10}$$

Figure 9.13 Two-dimensional projections of (a) the Arrhenius model and (b) the two-state model.

For simplicity, let $h = (\Delta H)/k$, $\alpha = \alpha_o/k$, and $\beta = \beta_o/k$. Suppose that there are $m \times n$ experimental data points for cell viability $C(u_\ell, t_\ell)$, $\ell = 1,\ldots, m \times n$ (i.e., m temperature measurement points with n exposure time for each temperature). Denote by z the function $z = \ln[(1 - C(u,t))/C(u,t)]$, then the data points (u_ℓ, t_ℓ, z_ℓ), $\ell = 1,\ldots, m \times n$ can be plotted in three-dimensional (3D) space with respect to $1/u$ and t.

At each point (u_ℓ, t_ℓ, z_ℓ), Equation (9.10) can be rewritten as

$$h\left(\frac{1}{u_\ell}\right) - \alpha t_\ell - \beta = z_\ell, \qquad \ell = 1,\ldots, m \times n \tag{9.11}$$

where parameters h, α, and β are to be determined by the standard least-squares regression using measurement data. Figure 9.13 illustrates that the transformation by introducing the z-variable converts a curved surface representing cell viability into a flat plane in 3D space. The 2D projections on the $C - 1/u$ and $C - t$ planes are also presented on Figure 9.13.

We summarize the algorithmic steps of parameter estimation for the two-state models as follows:

1. Compute $z_\ell = \ln[(1 - C(u_i, t_j))/C(u_i, t_j)]$, $i = 1,\ldots, m$; $j = 1,\ldots, n$; $\ell = 1,\ldots, m \times n$.
2. Plot data points z_ℓ versus time t and $1/u$ on a 3D graph.
3. Use bilinear regression to find the coefficients: h, α, and β.
4. The resulting coefficients are used directly in the model (Equation 9.4).

Since the range of $C(u,t) \in [0,1]$, we need to exclude initial points $C(u_i, 0) = 1$, $i = 1,\ldots, m$, in the least-squares regression process. This will not affect the final

results because the initial conditions in the original form (Equation 9.4) are automatically satisfied.

As a comparison, we also list the major steps to establish the Arrhenius model:

1. Plot data points $C(u_i,t_j)$ versus time for all $i=1,\ldots,m; j=1,\ldots,n$.
2. Determine time τ_i such that $C(u_i,\tau_i)=36.8\%(\Omega=1), i=1,\cdots,m$.
3. Plot data points $(\ln\tau_i, 1/u_i)$ on a 2D graph, $i=1,\ldots,m$.
4. Use linear regression to find the slope and $(\ln\tau)$-intercept.
5. The resulting slope is E_a/R, and the $(\ln\tau)$-intercept is $\ln A$.

Next, we discuss the major differences and similarities between two cell damage models.

9.6.3 Model Comparison between the Arrhenius Model and the Two-State Model

The *cell damage index* Ω is defined as usual. When the cell viability function $C(u,t)$ is normalized and $C(u,0)$ is set to one, we have $\Omega = -\ln C(u,t)$. Recall that the Arrhenius model assumes that the cell damage rate is proportional to the rate of reaction $k(u)=e^{-\frac{E_a}{Ru}}$. Thus, the cell damage index based on the Arrhenius model is

$$\Omega = \int_0^t A e^{\frac{-E_a}{Ru(\tau)}}\, d\tau \tag{9.12}$$

where t is the total exposure time and A is a constant that is often referred to as the frequency factor [49]. If temperature is kept constant during the entire exposure time t, then

$$\Omega = A\, t\, e^{\frac{-E_a}{Ru}} \tag{9.13}$$

In order to compare the Arrhenius model with the two-state model, we rewrite Equations (9.15) and (9.12) in terms of cell viability in a differential form:

$$\begin{cases} \dfrac{\partial C(u,t)}{\partial t} = -k(u)\cdot C(u,t) \\[2mm] \dfrac{\partial C(u,t)}{\partial u} = -\left(t k(u)\dfrac{E_a}{R}\right)\cdot\dfrac{C(u,t)}{u^2} \end{cases} \tag{9.14}$$

Therefore, the Arrhenius model is an approximation to the two-state model when $e^{-\Delta G/Ru} \ll 1$ with different choices of parameters.

Note that both functions $C(u,t)$ and $D(u,t)$ depend on ΔG, which is a function of temperature and time involving parameters that will be determined by experiments. In addition, it is important to recognize that the variable t is treated simply as a label for a continuous sequence of quasistatic states during heating.

9.7   SENSITIVITY STUDY

When creating a high-fidelity bioheat transfer model meant for prediction, a crucial element is capturing the heating source accurately. In the case of laser therapy, this mainly involves modeling the laser fluence in the tissue correctly. While there are two standard ways of modeling this—analytically or by using a Monte Carlo method—they both depend on three optical parameters of interest: the absorption coefficient, μ_a; the scattering coefficient, μ_s; and the anisotropic factor, g. Respectively, these give the average number of photons that are absorbed per unit length, the average number of photons scattered per unit length, and the expected value of the cosine of the scattering angle. In living tissue, each of these parameters is truly a function of space, light wavelength, and temperature. However, the way in which they are obtained experimentally usually limits them to functions of wavelength only, though the temperature can sometimes be accounted for. The model being presented in this chapter is currently implementing these parameters as functions of wavelength, and thus (since a single wavelength is used during treatment) leaving them constant throughout the entire simulation. Experiments have been done by Nau et al., however, showing that as the temperature increases, these parameters do not remain constant [61]. As the treatment being considered is meant to increase the temperature in the modeling region, it seems that this effect should most definitely be captured. However, the Pennes bioheat transfer model highly diffuses the heat in the domain. Thus, there is a question of whether the change in the heat source parameters will affect the overall heating profile enough to warrant modeling them as functions of temperature instead of constants. A sensitivity study was conducted to answer this question, the results of which are given here.

$$\Omega = \ln\left(\frac{C(u,0)}{C(u,t)}\right) \tag{9.15}$$

Laser fluence terms are generally obtained in one of two ways: analytically or via a Monte Carlo method. When capturing fluence analytically, a diffusion theory must be used, and generally many simplifying assumptions are made regarding boundary conditions and the source geometry. However, once the equation form is found, it is differentiable and easily calculated for different sets of parameters. Generally, the diffusion theory assumption, which states that the light radiance is mostly isotropic but for a small perturbation in one direction, holds when the source is not collimated and far from a boundary of two layers

with very different refraction indices or optical parameters (i.e., tissue and air). In contrast, the Monte Carlo method allows for a more accurate handling of boundary conditions and source geometries.

However, once the fluence is found for one set of parameters, there is no easy way to convert it into the fluence for another set of parameters; the entire simulation must be run again. Their differences make them appropriate or necessary for different situations; analytic solutions are appropriate for interstitial diffuse lasers, while Monte Carlo solutions are necessary, for high accuracy, when modeling laser beams incident to a flat surface.

In the experiments done for this research, despite the specific interest in interstitial tumors, both topical and interstitial lasers have been used. Since different source terms should be used for these situations, the sensitivity study presented here considers both an analytic solution as well as a Monte Carlo solution. In particular, the analytic fluence term considered is

$$\Phi(\mathbf{r}) = 3P(t)\mu_{tr} \frac{e^{-\mu_{eff}\mathbf{r}}}{4\pi\mathbf{r}}$$

where P is the power, $\mu_{tr} = \mu_a + (1-g)\mu_s$, and $\mu_{eff} = \sqrt{3\mu_a\mu_{tr}}$. This is derived as a solution to the transport equation as a spherically isotropic point source. The Monte Carlo fluence used follows the algorithm in Welch and van Gemert [62] incorporating a Gaussian initialization profile of a $1/r^2$ radius of 2 cm with 3 million photons for each simulation. For each of the source terms, the sensitivity was analyzed by running many simulations with each, varying one parameter while holding the others constant. Original values of parameters were $\mu_a = 2.15$ [1/cm], $\mu_s = 14.2$ [1/cm], and $g = 0.7$. The squared L^2 space–time norm of the temperature field was then calculated as the quantity of interest and plotted. The squared L^2 norm used is given here:
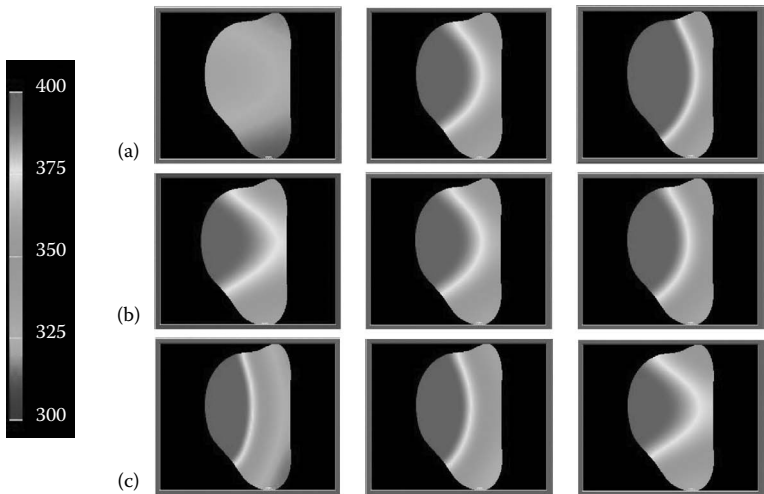
$$\int_0^T \int_\Omega |u(\mathbf{x},t)|^2 \, d\mathbf{x} \, dt$$

The different simulations were all run on a mesh representing a tumor on the leg of a mouse, a setup that is admittedly more appropriate for the Monte Carlo approach due to the boundary interface. Use of the isotropic source term, however, is not inappropriate for the purposes of this study since the general changes in the model's predictions are what are of interest. Figures 9.14 and 9.15 each show representative snapshots of the temperature profiles. The snapshots are each at time step 40, equivalent to 3 minutes and 20 seconds of heating.

The general effects of changing these parameters, which can be seen in Figures 9.14 and 9.15, are the same for both source terms. Higher values of μ_a and μ_s are associated with an increase in heating, whereas an increase in g is associated with a decrease in heating. However, the relative increase or decrease
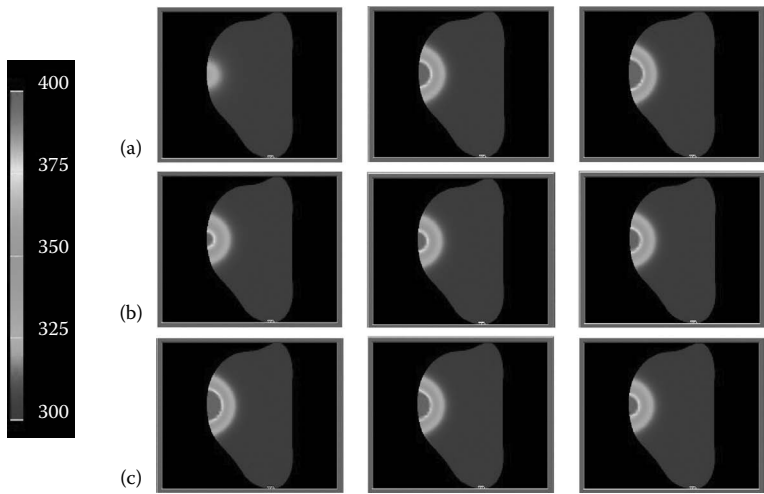
Figure 9.14 All images here show the temperature field generated with a Monte Carlo source term at time step 40, equivalent to 3 minutes and 20 seconds of heating. Line (a) contains images from simulations using values of $\mu_a = 0.44$, 3.14, and 5.0 [1/cm], respectively. Line (b) contains images from simulations using values of $\mu_s = 1$, 11, and 25 [1/cm], respectively. And line (c) contains images from simulations using values of $g = 0$, 0.5, and 0.99, respectively. Original values of the parameters are $\mu_a = 2.15$, $\mu_s = 14.2$, and $g = 0.7$. Temperature is given in degrees of Kelvin.

Figure 9.15 All images here show the temperature field generated with an isotropic source term at time step 40, equivalent to 3 minutes and 20 seconds of heating. Line (a) contains images from simulations using values of $\mu_a = 0.44$, 3.14, and 5.0 [1/cm], respectively. Line (b) contains images from simulations using values of $\mu_s = 1$, 11, and 25 [1/cm], respectively. And line (c) contains images from simulations using values of $g = 0$, 0.5, and 0.99, respectively. Original values of the parameters are $\mu_a = 2.15$, $\mu_s = 14.2$, and $g = 0.7$. Temperature is given in degrees Kelvin.
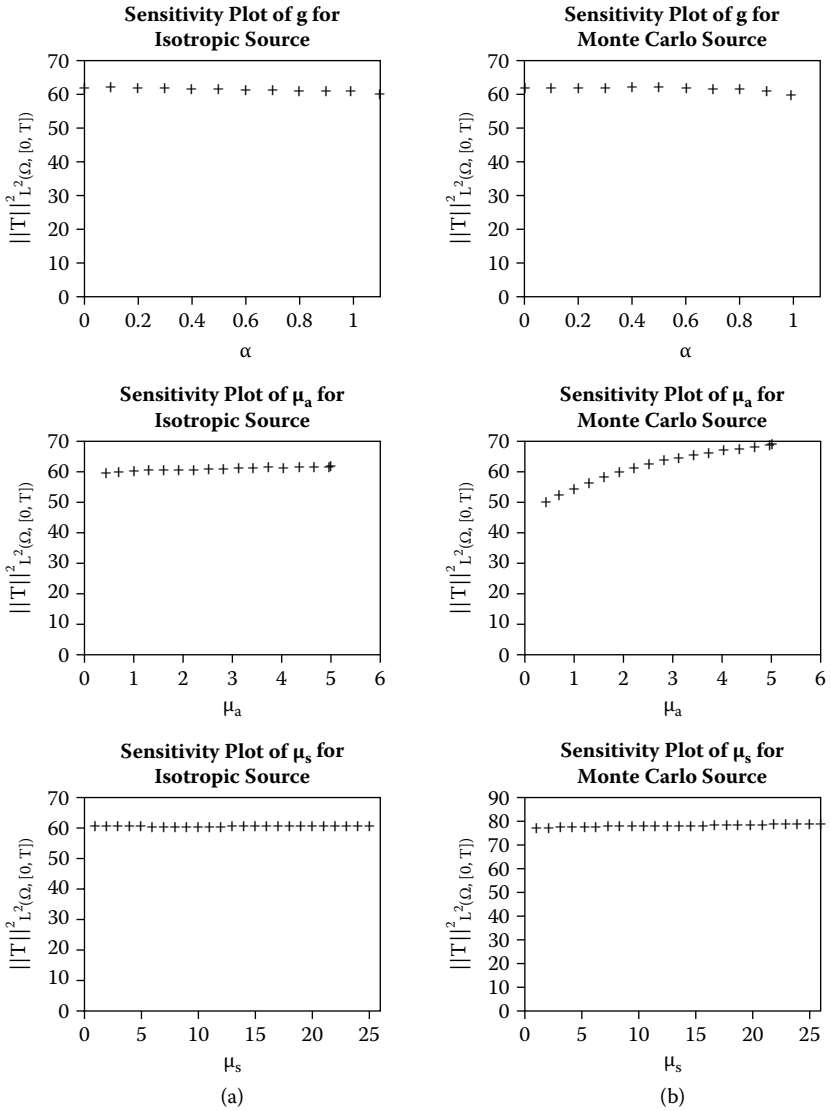
Figure 9.16 (a) Sensitivity plots for the isotropic source term simulations. (b) Sensitivity plots for the Monte Carlo source term simulations.

in temperature does appear to be different for the two source terms. The graphs in Figure 9.16a,b show the values of the quantity of interest, the L^2 norm, generated in each simulation and graphically show the general effects mentioned above. As a remark, the Monte Carlo simulations have produced more heating than the analogous isotropic simulations because the source is assumed to be 2 cm in diameter, whereas the isotropic source was merely at a point.

Table 9.1   Linear Regression Slopes of Plotted Sensitivities

	Monte Carlo	Isotropic
μ_a	4.95	0.398
μ_s	.071	0.017
g	−1.55	−1.09

These graphs indicate that the model's sensitivity to the parameters, for both source terms, is for the most part linear. For the range tested here, the linear regression slopes are given in Table 9.1. It can be argued from these results that in the isotropic case, both the parameters μ_s and μ_a may be treated as functions of wavelength only, but that g may need to be a function of temperature as well. However, in the Monte Carlo case, while μ_s can still remain just a function of wavelength, both μ_a and g should be dependent on temperature.

9.8   CONCLUSIONS AND FUTURE DIRECTIONS

Every aspect of the control system is operational and has been tested on a 1% agar phantom material. This testing represents a project milestone. The phantom material has provided an animal-free method of testing and debugging the entire control system. The phantom is meshed, it is registered, the computers in Austin control the heating, thermal images of the heating are acquired and sent to HP3d, HP3d calibrates and optimizes the model parameters, and, finally, a visualization of the entire process is provided in Houston. Figure 9.17a shows a particular time instance of heating of the phantom with an external collimated source. For

(a)   (b)
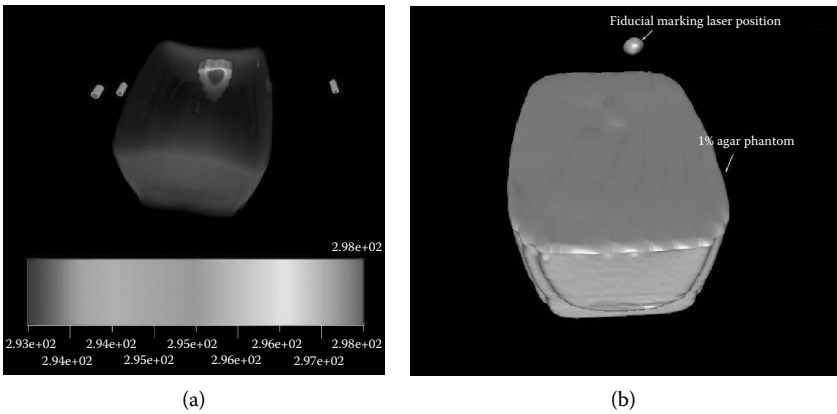
Figure 9.17   (a) 3D volume rendering of MRI and MRTI images at a selected time instance. The phantom geometry is shown in grayscale, and the thermal image is overlaid. The color bar illustrates the temperature range. (b) Isosurface visualization of MRI images of the geometry of the phantom material. The fiducial used to mark the laser probe for the FEM calculations are also shown.

this particular test, the thermal images were mainly used to periodically update the initial condition of the FEM computation in real time. After each update, the calculations proceeded to predict all the way to the end of the treatment. On current parallel computing architectures, the prediction capabilities seen are that 10 seconds of computation time at high-performance computing facilities provide ≈40 to 50 seconds' worth of prediction. Figure 9.17b conveys the geometry of the phantom, as seen by an isosurface visualization of the MRI images. A fiducial marking the external laser position is shown above the phantom. This is used to obtain the coordinates of the laser tip in the FEM calculations.

The next milestone on the horizon for this multidisciplinary effort is to perform an *in vivo* trial of the control system. Current results indicate that it is indeed feasible to accurately control the bioheat transfer through real-time imaging and computational prediction. The culmination of adaptive hp finite element technology implemented on parallel computing architectures, modern data transfer and visualization infrastructure, thermal-imaging modalities, and cellular damage mechanisms as cancer treatment tools will provide a very powerful methodology for planning and optimizing thermal therapy delivery for cancer treatments.

ACKNOWLEDGMENTS

REFERENCES

1. K. Shinohara, Thermal ablation of prostate diseases: advantages and limitations, *Int. J. Hyperthermia*, vol. 20, no. 7, pp. 679–697, 2004.
2. R. Salomir et al., Hyperthermia by MR-guided focused ultrasound: accurate temperature control based on fast MRI and a physical model of local energy deposition and heat conduction, *Magn. Reson. Med.*, vol. 43, no. 3, pp. 342–347, 2000.
3. F. C. Vimeux et al., Real-time control of focused ultrasound heating based on rapid MR thermometry, *Invest. Radiol.*, vol. 34, no. 3, pp. 190–193, 1999.
4. J. T. Oden, K. R. Diller, C. Bajaj, J. C. Browne, J. Hazle, I. Babuška, J. Bass, L. Demkowicz, Y. Feng, D. Fuentes, S. Prudhomme, M. N. Rylander, R. J. Stafford, and Y. Zhang, Dynamic data-driven finite element models for laser treatment of prostate cancer, *Num. Meth. PDE*, vol. 23, no. 4, pp. 904–922, 2007.
5. J. T. Oden and S. Prudhomme, Goal-oriented error estimation and adaptivity for the finite element method, *Comput. Math. App.*, vol. 41, nos. 5–6, pp. 735–756, 2001.
6. S. Balay, W. D. Gropp, L. C. McInnes, and B. F. Smith, *Petsc users manual*, Tech. Rep. ANL-95/11—Revision 2.1.5, Argonne, Ill.: Argonne National Laboratory, 2003.
7. S. J. Benson, L. C. McInnes, J. Moré, and J. Sarich, *TAO user manual* (revision 1.8), Tech. Rep. ANL/MCS-TM-242, Argonne, Ill.: Argonne National Laboratory, Mathematics and Computer Science Division, 2005. http://www.mcs.anl.gov/tao.

8. A. V. S. Inc., AVS user's guide, May 1992, National Congress on Computational Mechanics, San Francisco, conference presentation.

9. Z. Yu and C. Bajaj, A fast and adaptive algorithm for image contrast enhancement, in *Proceedings of IEEE International Conference on Image Processing*, pp. 1001–1004, 2004.

10. C. Bajaj, Q. Wu, and G. Xu, Level set based volumetric anisotropic diffusion, in *ICES Technical Report 301*, Austin: University of Texas at Austin, 2003.

11. J. Sethian, A marching level set method for monotonically advancing fronts, *Proc. Natl. Acad. Sci.*, vol. 93, no. 4, pp. 1591–1595, 1996.

12. Z. Yu and C. Bajaj, Normalized gradient vector diffusion and image segmentation, in *Proceedings of European Conference on Computer Vision*, pp. 517–530, 2002.

13. Z. Yu and C. Bajaj, A segmentation-free approach for skeletonization of gray-scale images via anisotropic vector diffusion, in *IEEE International Conference on Computer Vision and Pattern Recognition (CVPR'04)*, vol. 1, pp. 415–420, 2004.

14. S. M. Park, G. W. Gladish, and C. L. Bajaj, Artery-vein separation from thoracic CTA scans, *IEEE Trans. Med. Imag.*, pp. 23–30, 2006.

15. R. Araiza, M. Averill, G. Keller, S. Starks, and C. Bajaj, 3D image registration using Fast Fourier Transform, with potential applications to geoinformatics and bioinformatics, in *Proceedings of the International Conference on Information Processing and Management of Uncertainty in Knowledge-Based Systems IPMU06*, pp. 817–824, 2006.

16. W. Lorensen and H. Cline, Marching cubes: a high resolution 3D surface construction algorithm, in *Siggraph*, pp. 163–169, 1987.

17. T. Ju, F. Losasso, S. Schaefer, and J. Warren, Dual contouring of hermite data, in *Siggraph 2002, Computer Graphics Proceedings*, pp. 339–346, Reading, Mass.: ACM Press/ACM SIGGRAPH/Addison Wesley Longman, 2002.

18. T. K. Dey and S. Goswami, Tight cocone: a water-tight surface reconstructor, in *Proceedings of the 8th ACM Symposium on Solid Modeling and Applications*, pp. 127–134, 2003.

19. T. K. Dey and S. Goswami, Provable surface reconstruction from noisy samples, in *Proceedings of the 20th ACM-SIAM Symposium on Computational Geometry*, pp. 330–339, 2004.

20. C. Bajaj, G. Xu, and X. Zhang, Smooth surface constructions via a higher-order level-set method, in *Computer-Aided Design and Computer Graphics, 2007 10th IEEE International Conference*, Beijing, China, October 15–18, 2007.

21. T. K. Dey, J. Giesen, S. Goswami, and W. Zhao, Shape dimension and approximation from samples, *Discr. Comput. Geom.*, vol. 29, pp. 419–434, 2003.

22. T. K. Dey, J. Giesen, and S. Goswami, Shape segmentation and matching with flow discretization, in *Proceedings of the Workshop Algorithms Data Structures (WADS 03)* (F. Dehne, J.-R. Sack, and M. Smid, eds.), LNCS 2748, Berlin, Germany, pp. 25–36, 2003.

23. C. Bajaj, A. Gillette, and S. Goswami, Topology-based selection and curation of level sets, in *Topology-in-Visualization, Topo-in-Vis'07* (A. Wiebel, H. Hege, K. Polthier, and G. Scheuermann, eds.), pp. 45–58, Leipzig, Germany: Springer Verlag, 2009.

24. Y. Zhang, Y. Bazilevs, S. Goswami, C. L. Bajaj, and T. J. R. Hughes, Patient-specific vascular NURBS modeling for isogeometric analysis of blood flow, *Comp. Met. Appl. Mech. Eng. (CMAME)*, vol. 196, nos. 29–30, pp. 2943–2959, 2007.

25. S. Goswami, T. K. Dey, and C. L. Bajaj, Identifying flat and tubular regions of a shape by unstable manifolds, in *Proceedings of the 11th Symposium on Solid and Physical Modeling*, pp. 27–37, 2006.

26. Y. Zhang and C. Bajaj, Adaptive and quality quadrilateral/hexahedral meshing from volumetric data, *Computer Methods in Applied Mechanics and Engineering (CMAME)*, vol. 195, nos. 9–12, pp. 942–960, 2006.

27. C. Bajaj, J. Chen, and G. Xu, Modeling with cubic A-patches, *ACM Transactions on Graphics*, vol. 14, no. 2, pp. 103–133, 1995.

28. Y. Zhang, C. Bajaj, and B.-S. Sohn, 3D finite element meshing from imaging data, *CMAME Unstruct. Mesh Gen.*, vol. 194, nos. 48–49, pp. 5083–5106, 2005.

29. C. Bajaj and G. Xu, Smooth shell construction with mixed prism fat surfaces, *Geom. Model. Comp. Suppl.*, vol. 14, pp. 19–35, 2001.

30. Y. Feng, D. Fuentes, A. Hawkins, J. Bass, M. N. Rylander, A. Elliott, A. Shetty, R. J. Stafford, and J. T. Oden, Nanoshell-mediated laser surgery simulation for prostate cancer treatment, *Eng. Comp.*, DOI: 10.1007/s00366-008-0109-y, 2007.

31. K. R. Diller, J. W. Valvano, and J. A. Pearce, Bioheat transfer, in *The CRC Handbook of Mechanical Engineering*, 2nd ed. (F. Kreith and Y. Goswami, eds.), pp. 4-278–4-357, Boca Raton, Fla.: CRC Press, 2005.

32. Y. Zhang, Y. Bazilevs, S. Goswami, C. Bajaj, and T. J. R. Hughes, Patient-specific vascular NURBS modeling for isogeometric analysis of blood flow, *CMAME*, vol. 196, pp. 2943–2959, 2007.

33. K. R. Diller, Stress protein expression kinetics, *Annu. Rev. Biomed. Eng.*, vol. 8, pp. 403–424, 2006.

34. A. Horwich, Protein aggregation in disease: a role for folding intermediates forming specific multimeric interactions, *J. Clin. Invest.*, vol. 110, pp. 1221–1232, 2002.

35. M. N. Rylander, S. Wang, S. Aggarwal, and K. R. Diller, Correlation of HSP 70 expression and cell viability following thermal stimulation of bovine aortic endothelial cells, *J. Biomech. Eng.*, vol. 127, pp. 751–757, 2005.

36. A. Peper, C. A. Grimbergen, J. A. Spaan, J. E. Souren, and R. van Wijk, A mathematical model of the HSP70 regulation in the cell, *Int. J. Hypertherm.*, vol. 14, pp. 97–124, 1998.

37. R. A. Coss, Inhibiting induction of heat shock proteins as a strategy to enhance cancer therapy, *Int. J. Hypertherm.*, vol. 21, pp. 695–701, 2005.

38. D. Srinivasan, L. R Burbach, D. V. Daniels, A. P. D. W. Ford, and A. Bhattacharya, Pharmacological characterization of canine bradykinin receptors in prostatic culture and in isolated prostate, *Brit. J. Pharmacol.*, vol. 142, pp. 297–304, 2004.

39. P. D. Walden, M. Ittmann, M. E. Monaco, and H. Lepor, Endothelin-1 production and agonist activities in cultured prostate-derived cells: Implications for regulation of endothelin bioactivity and bioavailability in prostatic hyperplasia, *Prostate*, vol. 34, pp. 241–250, 1998.

40. D. M. Peehl, G. K. Leung, and S. T. Wong, Keratin expression: a measure of phenotypic modulation of human prostatic epithelial cells by growth inhibitory factors, *Cell Tiss. Res.*, vol. 277, pp. 11–18, 1994.

41. M. N. Rylander, K. R. Diller, S. Wang, and S. Aggarwal, Correlation of HSP70 expression and cell viability following thermal stimulation of bovine aortic endothelial cells, *J. Biomech. Eng.*, vol. 127, pp. 751–757, 2005.

42. S. Arrhenius, On the reaction velocity of the inversion of cane sugar by acids, *Zeitschrift für Physikalische Chemie*, vol. 4, p. 226, 1889.

43. K. J. Laidler, *Chemical Kinetics*, 3rd ed., New York: Harper & Row, 1987.

44. F. Henriques and A. Moritz, Studies of thermal injury. i. the conduction of heat to and through skin and the temperatures attained therein. A theoretical and an experimental investigation, *Am. J. Pathol.*, vol. 23, no. 53, pp. 1–549, 1947.

45. A. Moritz and F. Henriques, Studies of thermal injury. ii. The relative importance of time and surface temperature in the causation of cutaneous burns, *Am. J. Pathol.*, vol. 23, pp. 695–720, 1947.

46. X. He and J. Bischof, Quantification of temperature and injury response in thermal therapy and cryosurgery, *J. Biomech. Eng.*, vol. 31, pp. 355–422, 2003.

47. J. Roti Roti and K. Henle, Comparison of two mathematical models for describing heat-induced cell killing, *Radiat. Res.*, vol. 81, no. 3, pp. 374–383, 1980.

48. J. Lepock, How do cells respond to their thermal environment? *Int. J. Hypertherm.*, vol. 21, no. 8, pp. 681–687, 2005.

49. J. Pearce and S. Thomsen, Rate process analysis of thermal damage, in *Optical-Thermal Response of Laser-Irradiated Tissue* (A. J. Welch and M. J. C. van Gemert, eds.), pp. 561–606, New York: Plenum, 1995.

50. J. Philibert, Some thoughts and/or questions about activation energy and pre-exponential factor, *Def. Diffus. Forum*, vol. 249, pp. 61–72, 2006.

51. W. C. Dewey, L. Hopwood, S. Sapareto, and L. Gerweck, Cellular responses to combinations of hyperthermia and radiation, *Radiat. Biol.*, vol. 123, no. 2, pp. 463–474, 1977.

52. J. Bayer, J. Rädler, and R. Blossey, Chains, dimers, and sandwiches: melting behavior of DNA nanoassemblies, *Nano Lett.*, vol. 5, no. 3, pp. 497–501, 2005.

53. D. Nelson and M. Cox, *Lehninger Principles of Biochemistry*, 4th ed., New York: Worth, 2004.

54. H. Jung, A generalized concept for cell killing by heat, *Radiat. Res.*, vol. 106, no. 1, pp. 56–72, 1986.

55. W. Tsang, V. Bedanov, and M. Zachariah, Master equation analysis of thermal activation reactions: energy-transfer constraints on falloff behavior in the decomposition of reactive intermediates with low thresholds, *J. Phys. Chem.*, vol. 100, pp. 4011–4018, 1996.

56. K. Dill, Theory for the folding and stability of globular proteins, *Biochemistry*, vol. 24, no. 6, pp. 1501–1509, 1985.

57. X. He and J. Bischof, The kinetics of thermal injury in human renal carcinoma cells, *Annal. Biomed. Eng.*, vol. 33, no. 4, pp. 502–510, 2005.

58. C. Merlo, K. Dill, and T. Weikl, Φ values in protein-folding kinetics have energetic and structural components, *Proc. Natl. Acad. Sci.*, vol. 102, no. 29, pp. 10171–10175, 2005.

59. T. Weikl, M. Palassini, and K. Dill, Cooperativity in two-state protein folding kinetics, *Prot. Sci.*, vol. 13, no. 3, pp. 822–829, 2004.

60. Y. Feng, J. Oden, and M. Rylander, A statistical thermodynamics based cell damage models and its validation *in vitro*, *J. Biomech. Eng.*, vol. 130, no. 041016, pp. 1–10, 2008.

61. W. H. Nau, R. J. Roselli, and D. F. Milam, Measurement of thermal effects on the optical properties of prostate tissue at wavelengths of 1,064 and 633 nm, *Laser Surg. Med.*, vol. 24, no. 1, pp. 38–47, 1999.

62. A. J. Welch and M. J. C. van Gemert, *Optical-Thermal Response of Laser-Irradiated Tissue*, New York: Plenum, 1995.